Biogeosciences, 19, 4459–4477, 2022
https://doi.org/10.5194/bg-19-4459-2022

Biogeosciences
Open Access
EGU

The influence of near-surface sediment hydrothermalism on the TEX_{86} tetraether-lipid-based proxy and a new correction for ocean bottom lipid overprinting

Jeremy N. Bentley[1], Gregory T. Ventura[1], Clifford C. Walters[2], Stefan M. Sievert[3], and Jeffrey S. Seewald[4]

[1]Department of Geology, Saint Mary's University, Halifax, Nova Scotia B3H 3C3, Canada
[2]Bureau of Economic Geology, University of Texas at Austin, Austin, Texas, USA
[3]Biology Department, Woods Hole Oceanographic Institution, Woods Hole, Massachusetts, USA
[4]Marine Chemistry and Geochemistry Department, Woods Hole Oceanographic Institution, Woods Hole, Massachusetts, USA

Correspondence: Gregory T. Ventura (todd.ventura@smu.ca)

Received: 20 September 2021 – Discussion started: 18 November 2021
Revised: 3 July 2022 – Accepted: 29 July 2022 – Published: 15 September 2022

Abstract. The diversity and relative abundances of tetraether lipids produced by archaea and bacteria in soils and sediments are increasingly used to assess environmental change. For instance, the TetraEther indeX of 86 carbon atoms (TEX_{86}), based on archaeal isoprenoidal glycerol dialkyl glycerol tetraether (iGDGT) lipids, is frequently applied to reconstruct past sea-surface temperatures (SSTs). Yet, it is unknown how the ratio fully responds to environmental and/or geochemical variations and if the produced signals are largely the adaptive response by Thaumarchaeota to oceanographic effects associated with climate or seasonal temperature changes in the upper water column. We present the results of a four push-core transect study of surface sediments collected along an environmental gradient at the Cathedral Hill hydrothermal-vent system in Guaymas Basin, Gulf of California. The transect crosses a region where advecting hydrothermal fluids reach 155 °C within the upper 21 cm below the seafloor (cm b.s.f.) close to the vent center to near-ambient conditions at the vent periphery. The recovered iGDGTs closest to the vent center experienced high rates of turnover with up to 94 % of the lipid pool being lost within the upper 21 cm b.s.f. Here, we show that the turnover is non-selective across TEX_{86} GDGT lipids and does not affect the ratio independently. However, as evident by TEX_{86} ratios being highly correlated to the Cathedral Hill vent sediment porewater temperatures ($R^2 = 0.84$), the ratio can be strongly impacted by the combination of severe lipid loss coupled with the addition of in situ iGDGT production from archaeal communities living in the vent sediments. The resulting overprint produces absolute temperature offsets of up to 4 °C based on the TEX_{86}^{H} calibration relative to modern climate records of the region. The overprint is also striking given the flux of iGDGTs from the upper water column is estimated to be ∼ 93 % of the combined intact polar lipid (IPL) and core GDGT lipid pool initially deposited on the seafloor. A model to correct the overprint signal using IPLs is therefore presented that can similarly be applied to all near-surface marine sediment systems where calibration models or climate reconstructions are made based on the TEX_{86} measure.

1 Introduction

Archaeal and bacterial tetraether cellular membrane lipids represent a group of common and structurally diverse compounds frequently used to track the presence of living and dead microorganisms as well as geochemical and physical conditions within present-day and paleoenvironments (e.g., Schouten et al., 2002, 2004, 2013; Sturt et al., 2004; Hopmans et al., 2004; Weijers et al., 2007, 2014; Hollis et al., 2012; O'Brien et al., 2017). In this regard, the proportional abundances of these lipids form various prominent proxies for assessing environmental change through time. For example, TEX_{86} (TetraEther indeX of 86 carbon atoms; Schouten et al., 2002) is a widely used archaeal-lipid-based paleotemperature proxy for marine environments. The ratio measures

variations in the number of cyclopentyl rings for a select group of archaeal core lipids (CLs) (Fig. S1 in the Supplement) following the assumption that biphytanyl cyclization is an organismal response to changing sea-surface temperatures (SSTs). The proxy is therefore used in many regions around the world with TEX_{86} values typically ranging from 0.2–0.9 in marine settings (e.g., Huguet et al., 2006; Kim et al., 2008; McClymont et al., 2012; Tierney, 2014). The utility of TEX_{86} rests on the premise that iGDGTs found in ocean bottom sediments are almost exclusively produced by marine planktonic archaea that inhabit the epipelagic zone (Wakeham et al., 2003; Tierney, 2014; Besseling et al., 2019, 2020). Lipids are therefore required to be efficiently and continually transported from the upper water column to the underlying ocean floor to produce a fossil chemostratigraphic record of microbial response to changing SST conditions with time (Wuchter et al., 2005).

Since its introduction, the reliability of TEX_{86} to accurately track paleoclimate variations has been questioned. TEX_{86}-based SST estimates have been observed to substantially deviate from other temperature proxies (e.g., Huguet et al., 2006; Rommerskirchen et al., 2011; Seki et al., 2012, 2014). For example, over the past decade, considerable effort has been made to reconstruct the early Paleogene greenhouse climate system. However, TEX_{86} appears to significantly overestimate reconstructed SSTs (Hollis et al., 2012) relative to other proxies such as Mg/Ca or clumped isotopic compositions of foraminiferal calcite, as well as various climate models based on partial pressure of carbon dioxide (pCO_2) predictions (Lunt et al., 2012; Naafs et al., 2018). For late Neogene climate reconstructions, TEX_{86} has been shown to underestimate warming trends relative to the $U^{k'}_{37}$ alkenone-index-derived (Brassell et al., 1986) temperatures (Lawrence et al., 2020). The apparent SST offsets have been attributed to how the proxy's associated lipids change in relation to their environment and if these changes are regulated by internal adaptations within the archaeon or by an overarching community succession. In this regard, the debate surrounding these discrepancies largely centers on establishing responses to seasonal biases (e.g., Herford et al., 2006; Wuchter et al., 2006; Huguet et al., 2011); the development of adequate calibration methods (e.g., Kim et al., 2010; Pearson et al., 2013; Tierney et al., 2014); identifying lipid sourcing effects, including subsurface sediments origins for those used with the calculation of TEX_{86} (e.g., Lipp and Hinrichs, 2009); and physical, chemical, and ecological controls for archaeon iGDGTs cyclization (e.g., Elling et al., 2015; Qin et al., 2015; Hurley et al., 2016).

For non-thermal influences, the primary concern is what archaeal taxa produce iGDGTs and where they are sourced. To this end, most TEX_{86} lipids are thought to be produced by Marine Group I (MGI) planktonic Thaumarchaeota (Brochier-Armanet et al., 2008), which are most abundant below the photic and epipelagic zone (e.g., Karner et al., 2001). Within this context, many regions of the ocean floor may become highly impacted by colder, deeper water column inputs (e.g., Karner et al., 2001; Huguet et al., 2007; Lopes dos Santos et al., 2010; Kim et al., 2012a, b, 2015; Pearson et al., 2013; Ho and Laepple, 2016; Hurley et al., 2016; Lui et al., 2018; Sinninghe Damsté et al., 2018). Other non-thermogenic driving forces impacting the production, cyclization, and relative abundance of TEX_{86}-based lipids include organismal selectivity to specific growth phases and growth rates (Elling et al., 2014; Hurley et al., 2016), redox conditions (Qin et al., 2015), and the incorporation of iGDGT (isoprenoidal glycerol dialkyl glycerol tetraether) from archaeal communities living in the ocean floor sediments. With respect to the latter, Lipp and Hinrichs (2009) demonstrated that the production of intact polar lipid GDGTs ($_{IPL}$GDGTs) by ocean floor sediment microbial communities collected in the Peru Margin were distinctly different from upper-water-column-sourced CLs and that the conversion of this living pool to fossil lipids would shift TEX_{86} ratios to higher values. However, the overall impact may not be substantial, as Umoh et al. (2020) found little effect to the TEX_{86} paleoclimate ratio when examining surface sediments near hydrothermal-vent sites on the Southeast Indian Ridge in the southern Indian Ocean. Lengger et al. (2012, 2014) also reported no significant deviation between the TEX_{86} values in sediment cores collected near the oxygen minimum zone from that of the overlying water column in the Arabian Sea with near-linear degradation rates of both IPLs and CLs. All together, the iGDGT abundances recorded in a TEX_{86} sediment value may ultimately constitute a multi-variable data point – mixing lipid components that are themselves responses to temperature, organismal substrate, and metabolism dynamics, biozone niche partitions spanning from the ocean surface to the shallow sediment archaeal community, which ultimately become further attenuated by depositional and diagenetic processes.

While not an ideal location to create SST reconstructions, hydrothermal vents of sedimented ocean basins do represent an anomalous endmember to the vast expanse of ambient ocean floor sediment where paleoclimate reconstructions are commonly produced. The sedimented vent systems of Guaymas Basin, Gulf of California (Fig. 1), is one such site. The basin experiences high sedimentation rates ranging from 0.4–0.2 cm yr^{-1} (Gieskes et al., 1988) due in part to the high productivity of the upper water column. The ocean floor hydrothermally impacted surface sediments are also a location of active and diverse microbial communities with vents that are often covered by *Beggiatoa*-dominated microbial mats (e.g., McKay et al., 2012; Meyer et al., 2013; Teske et al., 2016). These sites should, in principle, enable a high-resolution archaeal-lipid stratigraphic record that provides optimal conditions for studying potential shallow diagenetic and subseafloor interferences to common archaeal-lipid-based environmental proxies. The region further offers an ideal setting to compare TEX_{86} proxy responses to in situ lipid production from thermophilic sedimentary ar-

chaea that differ from the pelagic background communities (e.g., Schouten et al., 2003). Recently, Bentley et al. (2022) produced a survey of the source and diagenetic and catagenetic alteration of archaeal lipids from the Cathedral Hill hydrothermal-vent complex (Fig. 1) in Guaymas Basin, Gulf of California. Within the investigation, it was observed that most iGDGTs are sourced from the overlying water column. Building on the results of Schouten et al. (2003), it was observed that these lipids can become heavily turned over in the hotter portions of the vent site where they rarely survive long enough to become cracked into hydrocarbon biomarkers such as biphytanes and derivatives of biphytanes. For this study, we further examine the iGDGT lipid distributions in these near-surface ocean floor sediments to determine if paleoclimate proxy signals can be impacted by the presence of subsurface archaeal populations. The distribution of iGDGTs and their corresponding environmental proxy signals were measured within the sediments along a transect at the complex. In this regard, this site offers the unique opportunity to evaluate the response of TEX_{86} and other tetraether-lipid proxies within a microbially diverse sedimentary environment that is exposed to high-temperature vent fluids.

2 Material and methods

2.1 Study location and sampling

Four sediment push cores were collected using HOV *Alvin* (dive 4462; 22 October 2008; human-occupied vehicle) at the Cathedral Hill hydrothermal-vent site, located at a water depth of 1996 m in the southern trough of Guaymas Basin, Gulf of California (27°0.629′ N, 111°24.265′ W) (Fig. 1). The push cores, labeled 1 to 4, were taken along a transect with ∼ 2 m spacing extending outwards from microbial-mat-covered sediments near the sulfide chimney complex to just outside of the microbial-mat area in ambient seafloor sediment. Thermal-probe measurements were sequentially taken beside each core (Table 1). Once the push cores were brought to the surface, the sediments were subsampled into 2–3 cm thick depth intervals, transferred to combusted glass vials, and immediately stored at −40 °C (on board the ship) before being shipped under dry ice to the laboratory and later freeze-dried and stored at −80 °C.

2.2 Lipid extraction

Lipid extractions followed a modified Bligh and Dyer protocol laid out in Bentley et al. (2022) and following Sturt et al. (2004). A subsample of freeze-dried sediment was added to a Teflon© centrifuge tube followed by the addition of 6 ml of mix A solvent solution comprising of 2 : 1 : 0.8 $v/v/v$ methanol (MeOH), dichloromethane (DCM), and phosphate buffer (5.5 g L^{-1} Na_2HPO_4; Avantor Performance Materials; adjusted to pH of 7.4 with HCl; Anachemia Canada Inc.). The solvent sediment mixture was further spiked with 1-alkyl-2-acetoyl-sn-glycero-3-phosphocholine (PAF) recovery standard purchased from Avanti Polar Lipids, Inc. The slurry was sonicated for 5 min then centrifuged for 5 min at 1250 rpm. The resulting supernatant was added to a separatory funnel. This procedure was performed twice before being joined by two replicate extractions using mix B, a 2 : 1 : 0.8; $v/v/v$ solution of MeOH, DCM, and trichloroacetic acid buffer (50 g L^{-1} $C_2HCl_3O_2$; Avantor Performance Materials, LLC; pH of 2), and finally two replicate extractions using mix C, a 5 : 1 v/v solution of MeOH and DCM. Once complete, this combined A, B, and C. For each step, the organic fraction was collected in a beaker, and the combination of mix A, B, and C was subjected to 10 ml of DCM and H_2O (Milli-Q) to achieve separation. The organic phase was drawn off, and the water was extracted using three DCM washes, drawing off the organic phase after each wash. The organic phase was back-extracted with H_2O to ensure purity. The resulting organic phase was then evaporated to dryness at 60 °C under dry nitrogen. The resulting total lipid extract (TLE) was transferred to pre-weighed autosampler vials using DCM : MeOH 1 : 1 v/v, spiked with 1, 2-diheneicosanoyl-sn-glycero-3-phosphocholine (C_{21}-PC; Avanti Polar Lipids, Inc.) and stored at −20 °C.

2.3 High-performance liquid chromatography–mass spectrometry (HPLC–MS)

Mass spectrometric analyses were performed on an Agilent Technologies 1260 Infinity II HPLC coupled to an Agilent Technologies 6530 quadruple time-of-flight mass spectrometer (qToF-MS) operated in positive mode. Chromatographic separation used a reverse-phase method outlined by Zhu et al. (2013). The HPLC was fitted with an Agilent Technologies ZORBAX RRHD Eclipse Plus C18 (2.1 mm × 150 mm × 1.8 µm) reverse-phase column and guard column maintained at 45 °C. The sample injection solvent was methanol. An aliquot of each sample representing 1 % of the TLE was analyzed. A 0.25 mL min^{-1} flow rate was established with mobile phase A consisting of methanol / formic acid / ammonium hydroxide (100 : 0.04 : 0.10 $v/v/v$) held at 100 % for 10 min, thereafter mixed following a linear gradient with mobile phase B of propan-2-ol / formic acid / ammonium hydroxide (100 : 0.04 : 0.10 $v/v/v$) to 24 %, 65 %, and 70 % over 5, 75, and 15 min intervals, respectively. Each sample run was finished by re-equilibrating the system with 100 % mobile phase A for 15 min. The effluent was ionized by an electrospray ionization source with a gas temperature of 300 °C, a 3 L min^{-1} drying gas flow, and a 5.33 µA source current. The mass spectrometer was set to a 100–3000 m/z scan range in positive mode in an untargeted method with 10 ppb resolution to simultaneously resolve both archaeal IPLs and CLs.

Analyte identification was achieved by accurate mass resolution, mass spectral analysis using Agilent Technologies's MassHunter software, and comparison of fragmenta-

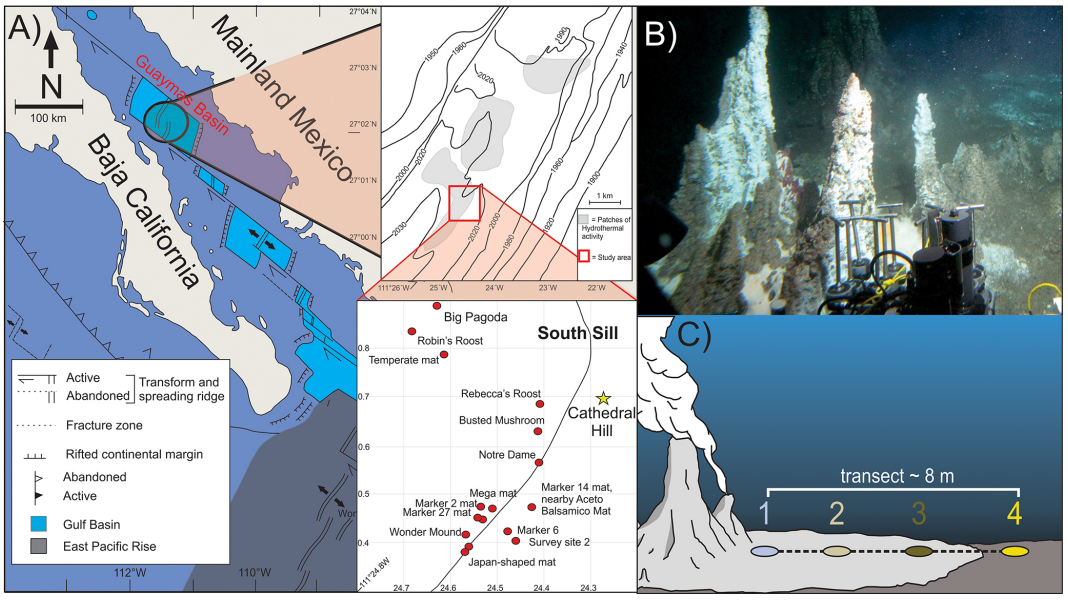

Figure 1. (a) Location map of Guaymas Basin and the southern sill (red outlined box) in the Gulf of California. Cathedral Hill is marked with a yellow star. **(b)** Photo of Cathedral Hill taken via HOV *Alvin*. **(c)** Schematic of the push-core transect with a color coding that is consistent for all plots throughout this paper. Maps modified from Teske et al. (2016), Dalzell et al. (2021), and Bentley et al. (2022).

tion patterns with the literature (e.g., Knappy et al., 2009; Liu et al., 2010; Yoshinaga et al., 2011; see Bentley et al., 2022, for further details). Mass fragments consistent with the loss of a biphytane (m/z 743.7) were screened for all archaeal lipids. Quantification was achieved by summing the integration peak areas of $[M+H]^+$, $[M+NH_4]^+$, and $[M+Na]^+$ adducts for the respective IPLs and CLs of interest. Concentration values were obtained relative to the internal C_{21}-PC standard and reported in microgram per gram dry sediment weight. Response factors were determined by a series of injections of a standard solution containing PAF; C_{21}-PC; 1,2-diacyl-3-O-(α-D-galactosyl1-6)-β-D-galactosyl-sn-glycerol (DGDG); 1,2-diacyl-3-O-β-D-galactosyl-sn-glycerol (MGDG); 1,2-di-O-phytanyl-sn-glycerol (archaeol); 1′,3′-bis[1,2-dimyristoyl-sn-glycero-3-phospho]-glycerol (14 : 0 cardiolipin) from Avanti Polar Lipids, Inc., USA; and 2,2′-di-O-decyl-3,3′-di-O-(1″,ω″-eicosanyl)-1,1′-di-(rac-glycerol) (C_{46}-GTGT) from Pandion Laboratories, LLC in amounts ranging from 100 pg to 30 ng. Response factors were calculated relative to the C_{21}-PC, and the appropriate correction factor was then applied to the lipid class of interest.

A series of samples were re-run to identify or confirm deviations in the data set. The variations between the concentrations of GDGTs in the re-run and the initial runs yielded a maximum difference of $\sim \pm 4\,\mu g\,g^{-1}$ per GDGT compound, providing confidence in the initial results and confirming the presence of two outliers in the data set (Bentley et al., 2022). These outliers are core 4 at 8–10 cm, with abnormally low concentrations of all compounds that are likely ion suppression from a sample heavily impregnated with oil, and core 3 at 15–18 cm, which contains relatively high lipid concentrations that are yet to be explained.

3 Results and discussion

3.1 Archaeal-lipid diversity and turnover

The Cathedral Hill transect sediments have iGDGTs containing 0–4 cyclopentyl (GDGT-0–4) as well as crenarchaeol (Cren) and the isomer of crenarchaeol (Cren') that contains five rings (four cyclopentyl and one cyclohexyl moiety) (Table S1). Branched GDGTs (brGDGTs) including Ia–c, IIa–c, and IIIa were found to have discontinuous and/or low absolute abundances, with some compound classes not being detected (i.e., brGDGT-IIIb; Table S2). The brGDGTs are therefore not further examined in this study. For cores 1 to 3 the concentrations of nearly all iGDGT compounds systematically decrease with depth (Fig. 2). Bentley et al. (2022) established the sedimentation of archaeal lipids from the upper water column as being uniform both in terms of spatial loading across the length of the transect as well as over an inferred 52.5–105 years of sedimentation as penetrated by the length of the push core (based on sedimentation rates). From this, it is estimated that $\sim 70.6 \pm 23.5\,\mu g$ iGDGT g^{-1} sed yr^{-1} is being deposited on the seafloor from the overlying water column. However, for cores closest to the vent site, lipid abundances exhibited a much sharper decrease with depth, which Bentley et al. (2022) attribute to the turnover of archaeal lipids cou-

Table 1. Cathedral Hill sample push core, sediment (sed), geochemical, and lipid proxy data.

Core[a]	Depth interval (cm b.s.f.)	HOV *Alvin* dive no. and core ID	Description/ lithology[b]	Porewater temperature (°C)[1]	Interpolated porewater temperature (°C)[1]	Sediment weight (g)[1]	TLE (mg g^{-1} sed)[1]	Sum of IPL iGDGT (µg g^{-1} sed)[2]	Sum of iGDGT (µg g^{-1} sed)[3]
1	0–2	GB4462-5	Black mud with microbial-mat filaments	19	19	1.97	11.5	16.7	503.1
1	2–4	GB4462-5	Brownish-green diatomaceous mud	–	67	2.04	7.65	14.6	461.7
1	4–6	GB4462-5	Brownish-green diatomaceous mud	85	85	2.03	9.37	6.0	203.3
1	6–8	GB4462-5	Brownish-green diatomaceous mud	–	105	1.99	2.09	4.3	148.6
1	8–10	GB4462-5	Brownish-green diatomaceous mud	–	117	2.01	4.38	3.2	59.0
1	10–12	GB4462-5	Grayish-green mud	121, 124	125	2.01	1.97	1.7	48.8
1	12–15	GB4462-5	Brownish-green consolidated mud with clay shards	–	135	1.98	1.99	1.4	78.7
1	15–18	GB4462-5	Brownish-green consolidated clay	142	145	1.96	1.69	0.0	42.6
1	18–21	GB4462-5	Brownish-green consolidated clay	153	153	1.98	1.72	0.0	38.4
2	0–2	GB4462-6	Black mud with microbial-mat filaments	9, 13	11	2.02	8.48	17.8	591.0
2	2–4	GB4462-6	Black mud with microbial-mat filaments	–	22	1.97	8.65	7.5	266.3
2	4–6	GB4462-6	Brownish-green diatomaceous mud	20	20	1.95	2.51	2.5	87.4
2	6–8	GB4462-6	Brownish-green diatomaceous mud	–	47	1.95	3.38	3.4	69.7
2	8-10	GB4462-6	Brownish-green diatomaceous mud	–	60	1.95	1.48	2.0	48.4
2	10–12	GB4462-6	Brownish-green diatomaceous mud	69, 77	73	1.94	4.19	2.0	52.1
2	12–15	GB4462-6	Brownish-green diatomaceous mud	–	87	2.02	1.69	1.0	44.2
2	15–18	GB4462-6	Brownish-green diatomaceous mud	118	105	1.95	2.01	0.0	22.3
2	18–21	GB4462-6	Brownish-green diatomaceous mud	109	125	1.94	1.38	0.0	31.2
3	0–2	GB4462-3	Black mud with microbial-mat filaments	3.2	3.2	1.96	7.31	15.3	511.3
3	2–4	GB4462-3	Brownish-green diatomaceous mud	–	8	1.96	3.91	8.3	308.9
3	4–6	GB4462-3	Brownish-green diatomaceous mud	15	15	2.00	2.86	7.0	283.5
3	6–8	GB4462-3	Brownish-green diatomaceous mud	–	26	2.02	5.00	7.5	275.3
3	8–10	GB4462-3	Brownish-green diatomaceous mud	34	34	1.97	2.02	5.7	251.1
3	10–12	GB4462-3	Brownish-green diatomaceous mud	–	43	2.01	1.86	5.8	227.7
3	12–15	GB4462-3	Brownish-green diatomaceous mud	–	54	1.94	1.78	6.5	184.6
3	15–18	GB4462-3	Brownish-green diatomaceous mud	61	66	2.01	1.43	12.3	473.1
3	18–21	GB4462-3	Brownish-green diatomaceous mud	83	80	1.96	1.98	5.2	182.3
4	0–2	GB4462-8	Black mud	0	0	1.93	3.44	16.7	485.4
4	2–4	GB4462-8	Brownish-green diatomaceous mud	1.5	8	2.01	3.17	14.6	417.8
4	4–6	GB4462-8	Brownish-green diatomaceous mud	16	16	1.95	4.00	6.0	480.6
4	6–8	GB4462-8	Brownish-green diatomaceous mud	–	18	2.02	4.19	4.3	359.7
4	8–10	GB4462-8	Brownish-green diatomaceous mud	–	21	2.02	4.76	3.2	153.5
4	10–12	GB4462-8	Brownish-green diatomaceous mud	–	23	1.95	4.84	1.7	459.5
4	12–15	GB4462-8	Brownish-green diatomaceous mud	–	25	1.95	5.74	1.4	515.2
4	15–18	GB4462-8	Sample lost during collection	–	–	–	–	0.0	503.1
4	18–21	GB4462-8	Sample lost during collection	29	–	–	–	0.0	461.7

pled to, but not directly caused by, hydrothermalism. For cores 1 and 2, losses reach as high as 94 % within the upper 21 cm b.s.f. (centimeters below seafloor). The lipid loss is less severe for core 3 at ∼ 60 %. For the ambient core 4, iGDGTs have similar downcore stratigraphic trends with a near-consistent average of 400 µg g^{-1} sed concentration and no systematic loss of lipids.

Due to the high-temperature conditions of the vent fluids at Cathedral Hill, the identified archaeal iGDGT-based IPLs within the sediments most likely represent the composition of cellular membrane material from archaeal communities living in the sediments. These lipids have exclusively monoglycosyl (1G) or diglycosyl (2G) head groups linked to a 2,3-sn-glycerol. Within the pyrolytic environment, the transformation of IPL iGDGTs could hypothetically add to the core iGDGT lipid pool. Similar to CLs, the 1G-GDGTs contain 0–4 cyclopentyl moieties and include Cren and Cren'. Surface concentrations of these lipids are ∼ 15 µg g^{-1} sed in cores 1 to 3 (residing within the microbial mat) and 11 µg g^{-1} sed for core 4 (Table S2). Also similar to the CLs, the archaeal IPL concentrations decrease downcore and are closely coupled to increasing porewater temperatures (Table S2). For cores 1 and 2, the maximum depths for detectable 1G-GDGTs are 15–18 and 12–15 cm b.s.f., corresponding to vent porewater temperatures of 145 and 87 °C, respectively. In core 3, 1G-GDGTs persist downcore with a consistent lipid depletion that reaches its lowest concentration of 5.2 µg g^{-1} sed in the bottom of the core at 18–21 cm b.s.f. sediment depth where porewater temperatures rise to 80 °C. In core 4, which is most similar to the ambient ocean bottom conditions and falls outside of the area covered by the microbial mat, the lipid concentrations average is ∼ 8 µg g^{-1} sed across the depth of the core. The 2G-GDGTs have zero to two cyclopentyl rings that for cores 1 and 2 are restricted to the upper 4 to 6 cm b.s.f. These lipids are not further investigated in this study, as 2G-GDGTs are of limited abundance (max summed concentrations <2 µg g^{-1} sed) and their structural diversities negligibly affect isoprenoid-based proxies.

Table 1. Continued.

Core[a]	Depth interval (cm b.s.f.)	HOV *Alvin* dive no. and core ID	Sum of TEX_{86} cGDGT[c] ($\mu g\ g^{-1}$ sed)	TEX_{86} cGDGT[c]	TEX_{86}^{H} cGDGT[d]	TEX_{86}^{H} reconstructed SSTs (Kim et al., 2010)[e]	RI[f]	MI[g]	TEX_{86} $_{IPL}$GDGT[c]
1	0–2	GB4462-5	110.7	0.56	−0.25	21.2	2.44	0.34	0.58
1	2–4	GB4462-5	117.1	0.58	−0.23	22.6	2.45	0.38	0.58
1	4–6	GB4462-5	47.7	0.58	−0.24	22.3	2.48	0.36	0.55
1	6–8	GB4462-5	33.0	0.58	−0.24	22.2	2.55	0.35	0.57
1	8–10	GB4462-5	13.0	0.59	−0.23	22.9	2.60	0.34	0.72
1	10–12	GB4462-5	10.1	0.57	−0.25	21.8	2.63	0.31	0.70
1	12–15	GB4462-5	17.8	0.61	−0.22	23.8	2.65	0.37	0.69
1	15–18	GB4462-5	9.8	0.61	−0.22	23.9	2.66	0.36	–
1	18–21	GB4462-5	9.3	0.63	−0.20	24.9	2.66	0.38	–
2	0–2	GB4462-6	128.5	0.55	−0.26	20.6	2.52	0.32	0.46
2	2–4	GB4462-6	58.2	0.54	−0.27	20.4	2.52	0.32	0.58
2	4–6	GB4462-6	19.2	0.54	−0.27	20.4	2.53	0.33	0.60
2	6–8	GB4462-6	13.4	0.56	−0.25	21.5	2.68	0.29	0.71
2	8–10	GB4462-6	9.3	0.58	−0.25	21.7	2.70	0.29	0.70
2	10–12	GB4462-6	10.1	0.57	−0.24	21.9	2.71	0.28	0.68
2	12–15	GB4462-6	8.5	0.57	−0.24	21.9	2.73	0.28	0.73
2	15–18	GB4462-6	4.5	0.58	−0.23	22.6	2.68	0.31	–
2	18–21	GB4462-6	6.0	0.59	−0.23	22.8	2.74	0.28	–
3	0–2	GB4462-3	127.0	0.54	−0.27	20.2	2.41	0.37	0.53
3	2–4	GB4462-3	57.7	0.53	−0.27	19.8	2.62	0.27	0.49
3	4–6	GB4462-3	60.0	0.53	−0.27	19.9	2.53	0.31	0.56
3	6–8	GB4462-3	59.8	0.54	−0.27	20.3	2.50	0.33	0.54
3	8–10	GB4462-3	53.0	0.53	−0.27	19.9	2.54	0.31	0.61
3	10–12	GB4462-3	42.1	0.54	−0.27	20.3	2.64	0.27	0.74
3	12–15	GB4462-3	39.2	0.56	−0.25	21.5	2.56	0.30	0.69
3	15–18	GB4462-3	86.8	0.55	−0.26	20.9	2.77	0.26	0.74
3	18–21	GB4462-3	36.4	0.57	−0.25	21.6	2.68	0.29	0.66
4	0–2	GB4462-8	112.9	0.54	−0.27	20.4	2.43	0.35	0.54
4	2–4	GB4462-8	85.3	0.53	−0.27	20.0	2.59	0.30	0.37
4	4–6	GB4462-8	102.7	0.54	−0.27	20.2	2.55	0.31	0.43
4	6–8	GB4462-8	70.8	0.52	−0.28	19.3	2.55	0.29	0.45
4	8–10	GB4462-8	26.6	0.53	−0.27	19.9	2.69	0.26	–
4	10–12	GB4462-8	91.0	0.53	−0.27	19.8	2.54	0.30	–
4	12–15	GB4462-8	73.7	0.53	−0.28	19.7	2.90	0.20	–
4	15–18	GB4462-8	110.7	–	–	–	–	–	–
4	18–21	GB4462-8	117.1	–	–	–	–	–	–

[1] Also reported in Bentley et al. (2022).
[2] Sum of GDGT-1, -2, -3. -4, -5, and -5′ (Table S1).
[3] Sum of all detected 1G- and 2G-GDGTs (Table S3).
[a] Collected core numbers are relabeled in the sample name to reflect a relative transect position (1–4).
[b] Sediment lithology based on freeze-dried sediments.
[c] TEX_{86} = (GDGT-2 + GDGT-3 + GDGT-5′)/(GDGT-1 + GDGT-2 + GDGT-3 + GDGT-5′) (Schouten et al., 2002) applied to both core GDGTs and 1-glycosyl-GDGTs (also referred to as $_{M}TEX_{86}$ in Sect. 3.4).
[d] TEX_{86}^{H} = log ((GDGT-2 + GDGT-3 + GDGT-5')/(GDGT-1 + GDGT-2 + GDGT-3 + GDGT-5')) for sediments outside low latitudes (Kim et al., 2010).
[e] Following the mean annual sea-surface calibration of 0 m water depth (SST = 68.4× TEX_{86}^{H} + 38.6) of Kim et al. (2010).
[f] Ring index (RI) = 0× (GDGT-0) +1× (GDGT-1) +2× (GDGT-2) +3× (GDGT-3) +4× (GDGT-4) +5× (GDGT-5)/ ΣGDGTs, adapted from Pearson et al. (2004) and promoted by Zeng et al. (2016).
[g] Methane index (MI) = (GDGT-1 + GDGT-2 + GDGT-3)/(GDGT-1 + GDGT-2 + GDGT-3 + GDGT-5 + GDGT-5′) by Zhang et al. (2011).

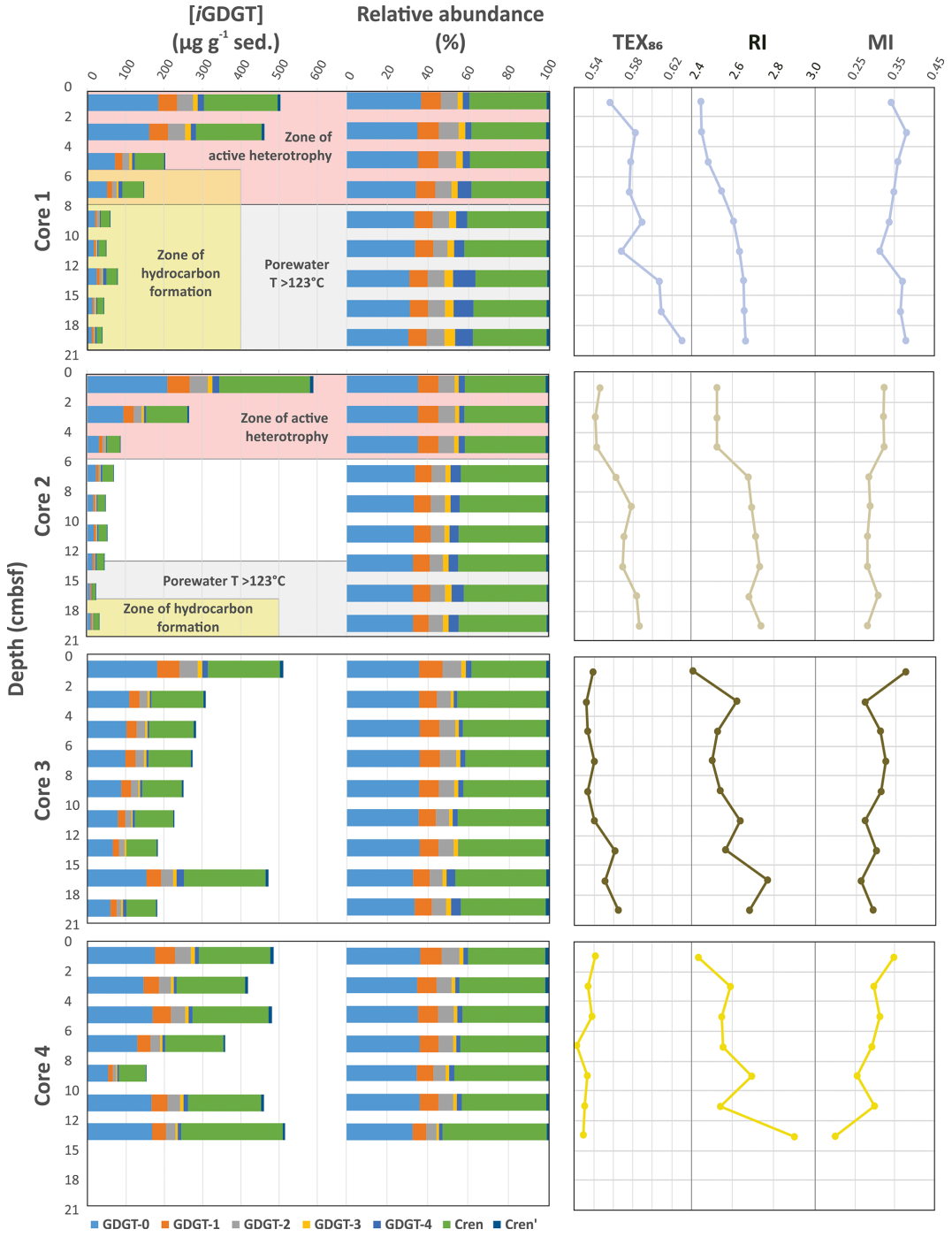

Figure 2. Downcore profiles of the Cathedral Hill core iGDGT absolute and relative lipid abundances and their generated iGDGT proxies: TEX_{86}, RI, and MI. The pink background indicates transect intervals within zones of active GDGT lipid heterotrophy (Bentley et al., 2022). The gray background indicates transect regions where porewater temperatures exceeded 123 °C, marking the known upper thermal limit of life (Kashefi and Lovley, 2003). Yellow fields are zones where oil generation and hydrocarbon degradation occur (Dalzell et al., 2021).

Lipid-based proxies for the calibration or reconstruction of paleoclimate records such as TEX_{86} are based on environmentally scaled contributions of select GDGT compounds. These proxies could be negatively impacted should other ocean floor sediment systems experience high rates of lipid turnover (Lengger et al., 2014). To evaluate whether downcore depletions of lipid concentrations impacted tetraether-based proxies, the concentrations of the highly abundant GDGT-0 was plotted relative to the TEX_{86} ratio lipids (iGDGT-1, iGDGT-2, iGDGT-3, and Cren') (Fig. 3a). For Fig. 3a, straight lines in the logarithmic plot indicate near-equal depletion rates between the paired x- and y-axis lipid classes. Similarly, parallel slopes for the various lipid pairs also indicate near-equal depletion rates, with vertical offsets between pairs marking different initial starting abundances of the compared lipid. In this regard, iGDGT-0, iGDGT-1, iGDGT-2, and Cren' have undergone the same rate of turnover. However, the depletion rate of iGDGT-3's is lower than that of other lipid classes for cores 1 and 2. Although, this may represent a distinct resilience to turnover, we suggest it instead results from overprinting by the subsurface hyperthermophilic-archaeal community (see below).

To better track changes across each core, the degradation rate constants (k') of TEX_{86} lipid classes were calculated for each push core (Fig. S2; Table S3) using a first-order kinetic model:

$$C_t = C_i \cdot e^{-k'}t, \quad (1)$$

in which C_t and C_i are concentration at time (t) and the initial concentration, respectively (e.g., Schouten et al., 2010). Rearranging Eq. (1), the k' values were calculated as

$$k' = (-\ln[C_t/C_i])/t, \quad (2)$$

from which data, it is evident that the downcore concentrations of each lipid decrease at equivalent rates (i.e., they have the same slopes for their rates of decay; $s^2 = 0.2$). The exception to this is core 2, which independent of two outliers has different decay paths for GDGT-3 and GDGT-5. This is consistent with the TEX_{86} iGDGT lipid classes largely being removed from the sediment lipid pool in a non-selective manner.

Based on these results, the TEX_{86}, ring index (RI), and methane index (MI) values were plotted against their respective summed iGDGTs lipid concentrations (Fig. 3b–d). For samples located within the habitable zone (having porewaters ranging from 0–123 °C; Kashefi and Lovley, 2003), no correlation is observed between the lipid abundances and proxy ratios of TEX_{86}, RI, or MI (Fig. 3b–d). This further suggests these proxies are not affected by turnover in the habitable zone. However, once sediment burial reaches beyond the habitable zone, TEX_{86} ratios trend to higher values (similarly also reflected in GDGT-3 concentration trends of Fig. 3a). Collectively, these data strongly indicate that archaeal-lipid turnover is largely nonselective of the TEX_{86} lipid classes and will therefore theoretically not in and of themselves significantly impact archaeal-lipid paleoclimate proxy reconstructions.

Apart from paleoclimate reconstructions, archaeal-lipid CLs are sometimes used to resolve aspects of localized biogeochemical cycles within sediments. To this end, the location and degree of anaerobic oxidation of methane (AOM) is determined by methane and archaeal-lipid carbon isotope measures (e.g., Boetius et al., 2000; Schouten et al., 2003; Stadnitskaia et al., 2008; Biddle et al., 2012) as well as by the proportional abundances of core GDGTs (cGDGTs) in the form of the MI (Zhang et al., 2011; Carr et al., 2018; Petrick et al., 2019). With respect to the latter, the MI proxy is used to differentiate regions of normal marine (with values between 0–0.3) and active AOM conditions in and around cold seeps (where values > 0.5–1 are reported for gas hydrate impacted sediments and subsurface environments with high AOM levels). To our knowledge, the use of this proxy for hydrothermal-vent systems has not been thoroughly investigated even though this microbial process has been well documented at Guaymas Basin. For example, highly ^{13}C-depleted CLs reaching up to $-70\,‰$ in hydrothermal-vent sediments with porewater temperatures as high as 95 °C indicate thermophilic archaea actively engaging in AOM (Schouten et al., 2003). Biddle et al. (2012) through the detection of relevant archaeal communities by 16S RNA in conjunction with highly depleted methane carbon isotope values determined active AOM spanning 35 to 90 °C porewater conditions. AOM is not likely to be the dominant form of carbon and sulfur metabolism, as it generally accounts for less than 5 % of sulfate reduction (Kallmeyer and Boetius, 2004). When applying the MI to the Cathedral Hill push-core transect survey, low values (ranging from 0.2–0.38; Table 1) are recorded with no correspondence to thermal controls across the vent transect (Fig. 4). Although, it could be considered that the low values arise from a lack of AOM within these sediments, the low MI values are consistent with a high upper-water-column iGDGT loading as estimated by Bentley et al. (2022).

3.2 TEX_{86} and reconstructed SSTs

McClymont et al. (2012) reported a GDGT-based reconstructed annual SSTs of 16–18 °C from particulate organic matter collected in ambient sediment traps in Guaymas Basin during an annual cycle from 1996–1997. The reconstructed temperatures followed the calibration model for sediments outside of polar regions proposed by Kim et al. (2010). These authors demonstrated the temperatures derived from the TEX_{86} reconstruction were significantly lower than those produced by the closely co-varying $U^{k'}_{37}$ paleoclimate proxy and satellite-measured estimates that jointly estimated a mean annual sea-surface temperature (MASST) of 23 °C. The longer 21-year (1982–2004) satellite-derived MASST is also reported to be higher at 24 °C (Herrera-Cervantes et al., 2007). Although, the sites and timeframes of these surveys

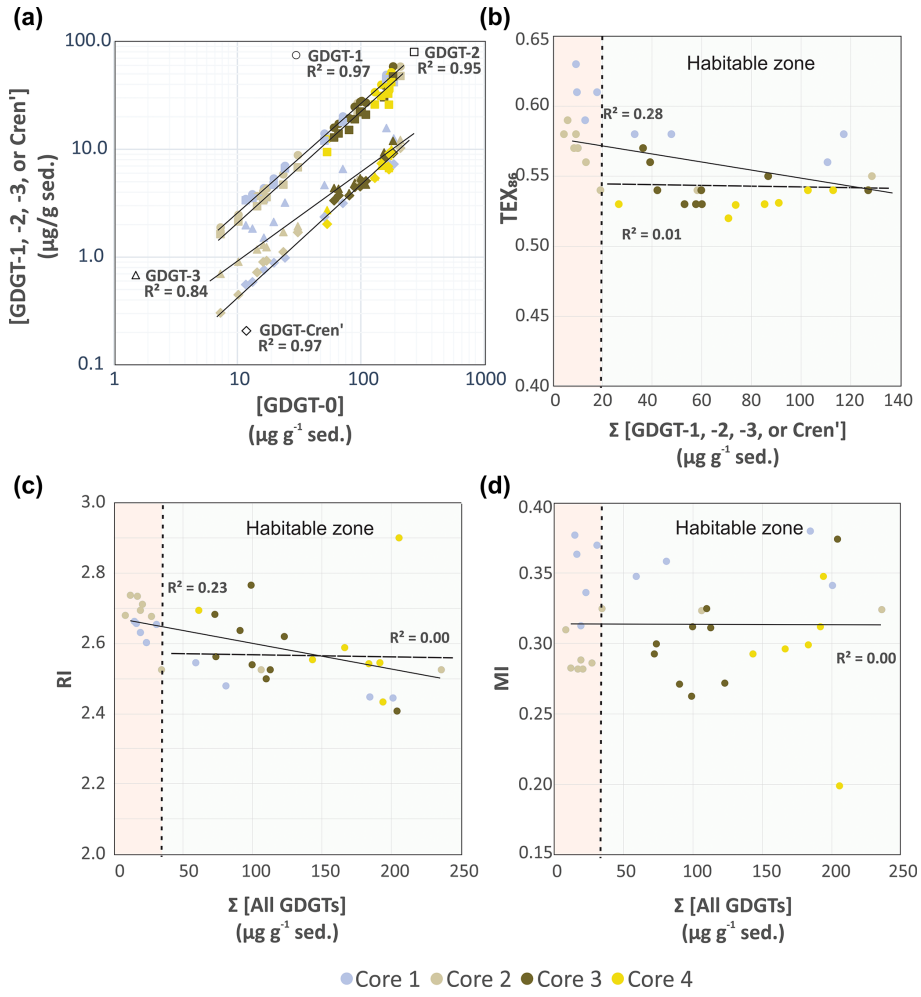

Figure 3. **(a)** Comparison of TEX_{86} lipid concentrations GDGT-1 (circles), GDGT-2 (squares), GDGT-3 (triangles), and Cren' (diamonds) relative to GDGT-0. Comparison of **(b)** TEX_{86}, **(c)** RI, and **(d)** MI proxy values relative to summed iGDGT abundances of the Cathedral Hill transect cores. Light-green and pink regions indicate areas within and outside the habitable zone of life. Solid and dashed regression lines mark the total number of samples investigated for this study ($n = 34$) and those that only reside within the habitable zone where up to 94 % of the archaeal-lipid turnover occurs ($n = 22$), respectively.

do not match that of the Cathedral Hill survey, they do provide context to what our reconstructed TEX_{86} values should record.

The high sedimentation rate at Cathedral Hill has resulted in near-homogenous inputs of organic matter from the upper water column across the transect area (Dalzell et al., 2021; Bentley et al., 2022). Therefore, TEX_{86} reconstructions should produce equivalent cross-transect trends with sediment depth. Nonetheless, as with changes in the archaeal-lipid concentrations, the profiles of iGDGT proxies TEX_{86} and RI of the transect similarly have downcore trends (Fig. 2; Bentley et al., 2022). For core 4, TEX_{86} spans a narrow range of values ($n = 7$; 0.52–0.54, average: 0.53 ± 0.01; Fig. 4a) across a period of $\sim$ 37.5 to 75 years, corresponding to the depth of the cores. To a slightly lesser degree, the core top (0–2 cm b.s.f.) across the transect also display near-equal values to core 4 ($n = 4$; 0.56–0.54; average: 0.55 ± 0.01). These values mark a TEX_{86}^{H} reconstructed mean annual SST of 19.3–20.4 °C following the Kim et al. (2010) calibration model (Table 1). However, the TEX_{86} values recorded in cores 1 to 3 at Cathedral Hill have considerably larger ranges with values spanning from 0.53 to 0.63 (Table 1) that systematically increase with rising porewater temperatures ($R^2 = 0.83$; Table 1; Figs. 2 and 4a). This increase is most noticeable in core 1 where the highest TEX_{86} values are obtained from the bottom core sediments (10–21 cm b.s.f.; marking the non-habitable zone), where TEX_{86} values span 0.57–0.63 (Table 1; Fig. 4a), corresponding to a TEX_{86}^{H} reconstructed SST change of 3.1 °C, marking a range from 21.8 to 24.9 °C (Table 1). The fundamental driver for the proxy is likely influenced by the archaeal community composition

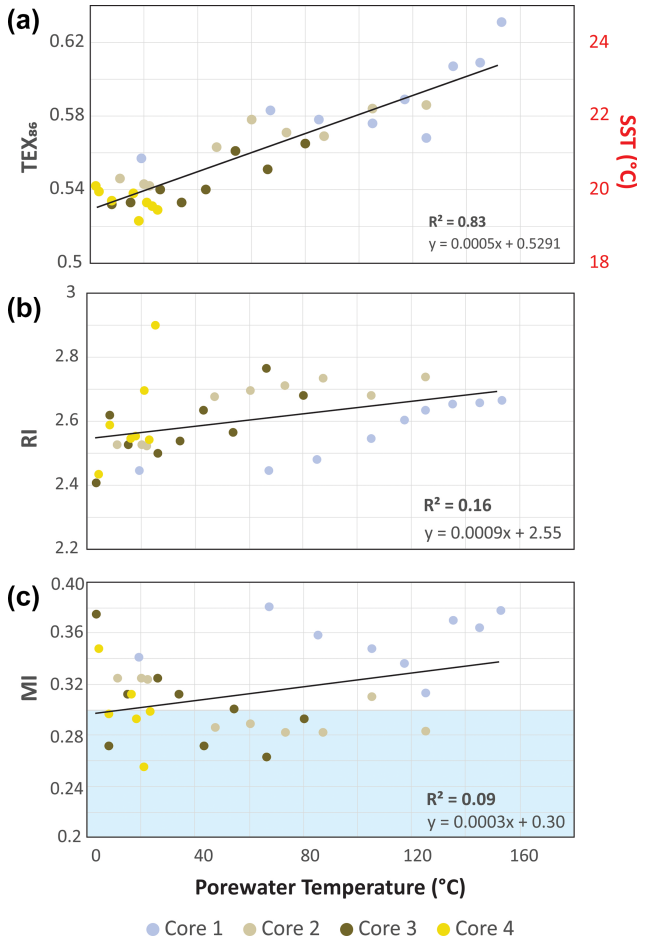

Figure 4. Cross plots of **(a)** TEX_{86}, **(b)** RI, and **(c)** MI; iGDGT proxies versus porewater temperature. TEX_{86}^{H} reconstructed MASSTs are based on Kim et al. (2010). Blue field indicates MI values for normal marine conditions (Zhang et al., 2011, 2016).

that is responding to their exposure to in situ vent fluid temperatures (Fig. 4).

Two mechanisms are considered for the observed proxy variations. The first is that progressive ring loss due to carbon–carbon bond cleavage of pentacyclic rings moieties by exposure to the sharp geothermal gradient acts to systematically attenuate the iGDGT lipid pool. Hydrous pyrolysis experiments conducted by Schouten et al. (2004) demonstrated that at extreme temperatures (ca. $> 160\,°C$), TEX_{86} values become negatively impacted by the preferential destruction of polycyclic GDGTs. Such losses produce progressively lower ratio values. Although the transect sediment porewaters do not reach the pyrolytic temperatures of the Schouten et al. (2004) experiment, they are high enough to generate hydrocarbons (Dalzell et al., 2021) and thermochemically degrade iGDGTs in the hottest regions of the transect; they are also more long-lived than what is produced from a laboratory experiment. However, the observed stratigraphic TEX_{86} trends do not match those of predicted ring loss, as the values increase rather than decrease in relation to elevated porewater condition. Nonetheless, the thermochemical oxidative loss of GDGTs and its effect on the TEX_{86} ratio is further explored below (Sect. 3.4).

The second mechanism is that subsurface microbial communities donate enough core GDGTs to overprint the detrital signal source. The RI (Fig. 4b) values were similarly compared to recorded porewater temperatures to better interpret the TEX_{86} trends and to ensure that the Cathedral Hill reconstructed temperatures are influenced by the subsurface microbial community. In this regard, RI is used to monitor the adaptive response of an archaeal community at the hydrothermal-vent site. Lipid cyclization is an adaptive response to changing environmental temperature or acidity in which an archaeon increases its rigidity by decreasing the fluidity and permeability of its cellular membrane that, therefore, also further regulates the flow of solutes and nutrients in and out of the cell (Gliozzi et al., 1983; De Rosa and Gambacorta, 1988; Uda et al., 2001; Schouten et al., 2002; Macalady et al., 2004; Boyd et al., 2013). Both cores 1 and 2 have RI values highly correlated to temperature ($R^2 = 0.87$ and 0.75, respectively), consistent with heat stress adaption. This same was also observed in Guaymas Basin by Schouten et al. (2003), who reported an increase in the RI of core lipid GDGTs with in situ temperature. As such, a significant proportion of the measured iGDGTs likely emanates from archaeal communities living in the shallow sediments of Cathedral Hill. As such, the lipid cyclization pattern may reflect stratigraphically discrete thermophilic to hyperthermophilic communities that are selectively adapted to more extreme temperature conditions (see Bentley et al., 2022, for further discussion on the lipid-based taxonomic makeup of the vent site).

3.3 Lipid signal sourcing

To evaluate the sources of measured archaeal lipids, CL and $_{IPL}TEX_{86}$ (the ratio applied to IPLs that contain equivalent core lipids) indices were compared as signal responses from their respective pools of living and dead cellular debris (Fig. 5). For cores 1, 2, and 3 the 1G-iGDGT $_{IPL}TEX_{86}$ measures are positively correlated with temperature ($R^2 = 0.46$, 0.74, and 0.66, respectively; Fig. 5a). In this regard, 1G-iGDGT $_{IPL}TEX_{86}$ ratio appears to be largely influenced by in situ porewater temperatures as well as potentially the archaeal community ecology of the vent system. Factors such as community composition and adaptation may further impact the $_{IPL}TEX_{86}$ ratio as the rates of changes between cores 1–3 are not the same. Similar to the $_{CL}TEX_{86}$ values, the $_{IPL}TEX_{86}$ is not correlated to their summed TEX_{86} lipid abundances (Fig. 5b). Such a condition is largely consistent with the living lipid pool being modified by the archaeal community's response to thermal stress and not by subse-

quent thermal–oxidative transformation occurring shortly after cell death.

The IPL and CL lipids of transect samples can be further grouped into three clusters (A, B, C), suggesting a mixed signal for the sourcing of archaeal GDGTs from both the living and dead pools of archaea (Fig. 5c), closely tracking temperature. In this plot, we assume that clusters falling on the 1 : 1 line indicate the living biota can equally contribute to the dead pool of total recovered GDGTs. Those off axis contribute either less or more to one or the other lipid pool. The three clusters mark unique thermal zones within the transect area, with cluster A being composed of the ambient core 2 to 4 seafloor surface samples, cluster B marking a mix of intermediate temperature samples from all cores, and cluster C being composed of high-temperature samples. The lipid groups likely mark distinct archaeal communities. As cluster B resides on the 1 : 1 line, the TEX_{86} core lipids likely have a mix of detrital and in situ inputs. Cluster C, however, appears likely dominated by in situ lipid production. The thermal zonation and equivalent directionality of the resulting ratios (i.e., both CL and $_{IPL}TEX_{86}$ ratios increase with porewater temperature) further support overprinting of the original $_{CL}TEX_{86}$ sea-surface signal by the ocean bottom sediment archaeal community as a mechanism for the observed $_{CL}TEX_{86}$ trends.

Collectively, these results suggest the source of the archaeal CLs measured in the TEX_{86} and RI indices progressively become more dominated by subsurface microbial communities adapted to the hotter hydrothermal-vent fluids. Our results also indicate that in select natural environments, such as hydrothermal-vent complexes, the TEX_{86} SST proxy may entirely record ocean bottom sediment porewater temperatures. To our knowledge, a clear case of overprinting to this level has not yet been demonstrated.

3.4 TEX_{86} overprint corrections

The measured TEX_{86} ($_{M}TEX_{86}$) value of the Cathedral Hill sediments is herein considered to be a weighted sum of a sea-surface TEX_{86} ($_{SS}TEX_{86}$) value acquired from lipids sourced in the upper water column that is further modified by a component of the deeper-water-column-sourced core lipids ($_{WC}TEX_{86}$) as well as by additions of archaeal lipids from the benthic and subsurface microbial communities ($_{Sed}TEX_{86}$). These ratio loadings are collectively also potentially further modified by diagenetic influences in the ocean bottom sediments. Over the cumulative sediment burial period and in consideration of the measured porewater temperatures of the Cathedral Hill push-core sediments, these influences include the selective loss of lipids by their binding into protokerogen (K) and by potential changes due to the loss of lipid by turnover (φ; Sect. 3.1 φ). Additional catagenetic effects from thermochemical alteration of lipids (θ) may also attenuate the sum of sedimentary core lipids by their exposure to high-temperature vent fluids. Collectively, these effects are considered to form the following relationship:

$$_{M}TEX_{86} = \frac{a_{SS}TEX_{86} + b_{WC}TEX_{86} + c(d_{0-n})_{Sed}TEX_{86}}{\varphi + K + \theta}, \quad (3)$$

where a, b, and c, are measured scaling parameters for lipid loading and φ, K, and θ are diagenetic and catagenetic alteration parameters. Solving for $_{SS}TEX_{86}$,

$$_{SS}TEX_{86} = \frac{_{M}TEX_{86}(\varphi + K + \theta)}{a} - \frac{b_{WC}TEX_{86} + c(d_{0-n})_{Sed}TEX_{86}}{a}. \quad (4)$$

In this regard, a portion of the archaeal community from the upper water column, presumably initially sourced of IPLs, and an additional community inhabiting the ocean floor sediments were assumed to eventually die, with their respective IPLs gradually hydrolyzing, joining the CL pool where they further contribute to the observed $_{M}TEX_{86}$ value. For this study, no data were collected to calculate $b_{WC}TEX_{86}$, and its potential impact on $_{M}TEX_{86}$ cannot be further considered in this study. However, it is highly likely, given the longer residence times for glycosidic-based head groups of the identified archaeal IPLs and their relatively short settling time through the water column (Lengger et al., 2012; Xie et al., 2013), that a component of this lipid source was already mixed with the $_{Sed}TEX_{86}$ contribution. For this study, $_{Sed}TEX_{86}$ is an $_{IPL}TEX_{86}$ ratio based on detected 1G-GDGT-1, 1G-GDGT-2, 1G-GDGT-3, Cren', 2G-GDGT-1, and 2G-GDGT-2, as present in the original paleoclimate proxy (Table 1; Fig. 6). Testing the removal of 2G-GDGT lipids, which have a low absolute concentration ($< 2\,\mu g\,g^{-1}$ sed) and shallow stratigraphic zones of occurrence (Sect. 3.1; Table S2), yielded a negligible $<1\,^{\circ}C$ change in the summed average reconstructed SST.

The $c(d_{0-n})$ measured scaling parameter was calculated as

$$c(d_{0-n}) = \sum_{i=0}^{n}\left(\frac{\left[GDGTs_{IPL-TEX_{86}\ lipids}\right]_n}{\left[GDGTs_{CL-TEX_{86}\ lipids}\right]_{0-2\ cm\ b.s.f.}}\right) \quad (5)$$

using the accumulated summed concentrations of 1G-GDGTs and 2G-GDGTs that have the potential to become converted to cGDGTs by progressive burial diagenesis and d_{0-n} marking the range of sampled sediment depths, with 0 being the 0–2 cm b.s.f. core top and n being the deepest point of sediment burial. These intervals are divided by the water column input of TEX_{86} lipids ($[GDGTs_{CL-TEX86\ lipids}]_{0-2\ cm}$) estimated to be $120\,\mu g\,g^{-1}$ sed based on their average measured concentration across the four-core transect. The function assumes the surface sediment does not hydrolyze its $_{IPL}$GDGTs to CLs (Table 2). When applied to Eq. (4) and further excluding φ, K, and θ, the $_{SS+WC}TEX_{86}^{H}$ reconstructed SSTs average $19.68 \pm 0.79\,^{\circ}C$ (Table 2; Fig. 6a), with the total samples having an unchanging depth profile that mirrors the range of values measured in the ambient sediments of core 4 (Fig. 2).

Table 2. Reconstructed sea-surface temperatures.

Sample	Depth (cm b.s.f.)	Porewater temperature (°C)	t time (years)	$_{M}TEX_{86}$ (measured iGDGT TEX_{86})	TEX_{86}^{H} reconstructed SST (°C)	TEX_{86} 1G-, 2G-GDGT IPLs ($\mu g\ g^{-1}$)	Cumulative 1G-, 2G-GDGT loading with depth ($\mu g\ g^{-1}$)	$_{Sed}TEX_{86}$ (i.e., 1G-, 2G-GDGT $_{IPL}TEX_{86}$)	$c(d_{0-n})$ cumulative weighted IPL loading (Eq. 5)
Core 1 (0–2cm)	1	19	10	0.56	21.2	4.80	0	0.58	0.00
Core 1 (2–4 cm)	3	67	20	0.58	22.6	3.41	4.80	0.58	0.04
Core 1 (4–6 cm)	5	85	30	0.58	22.3	1.29	8.21	0.55	0.07
Core 1 (6–8 cm)	7	105	40	0.58	22.2	1.14	9.50	0.57	0.08
Core 1 (8–10 cm)	9	117	50	0.59	22.9	1.41	10.64	0.72	0.09
Core 1 (10–12 cm)	11	125	60	0.57	21.8	0.76	12.05	0.70	0.10
Core 1 (12–15 cm)	13	135	70	0.61	23.8	0.72	12.81	0.69	0.11
Core 1 (15–18 cm)	17	145	80	0.61	23.9	0.00	13.53	0.69*	0.11*
Core 1 (18–21 cm)	20	153	90	0.63	24.9	0.00	13.53	0.69*	0.11*
Average				0.59	22.84				
SD				0.02	1.16				
Core 2 (0–2 cm)	1	11	10	0.55	20.6	4.33	0	0.49	0.00
Core 2 (2–4 cm)	3	22	20	0.54	20.4	1.80	4.33	0.57	0.04
Core 2 (4–6 cm)	5	20	30	0.54	20.5	0.76	6.13	0.60	0.05
Core 2 (6–8 cm)	7	47	40	0.56	21.5	1.31	6.89	0.73	0.06
Core 2 (8–10 cm)	9	60	50	0.58	22.3	0.88	8.20	0.70	0.07
Core 2 (10–12 cm)	11	73	60	0.57	22.0	0.92	9.08	0.68	0.08
Core 2 (12–15 cm)	13	87	70	0.57	21.8	0.40	10.00	0.73	0.08
Core 2 (15–18 cm)	17	105	80	0.58	22.6	0.00	10.40	0.73*	0.09
ore 2 (18–21 cm)	20	125	90	0.59	22.7	0.00	10.40	0.73*	0.09*
Average				0.56	21.61				
SD				0.02	0.91				
Core 3 (0–2 cm)	1	3.2	10	0.54	20.2	3.51	0	0.56	0.03
Core 3 (2–4 cm)	3	8	20	0.53	19.9	1.79	3.51	0.51	0.01
Core 3 (4–6 cm)	5	15	30	0.53	19.9	1.45	5.30	0.57	0.01
Core 3 (6–8 cm)	7	26	40	0.54	20.3	1.77	6.74	0.55	0.01
Core 3 (8–10 cm)	9	34	50	0.53	19.9	1.70	8.51	0.61	0.01
Core 3 (10–12 cm)	11	43	60	0.54	20.3	2.16	10.21	0.71	0.02
Core 3 (12–15 cm)	13	54	70	0.56	21.4	2.52	12.37	0.69	0.02
Core 3 (15–18 cm)	17	66	80	0.55	20.9	4.72	14.89	0.73	0.04
Core3 (18–21 cm)	20	80	90	0.57	21.6	2.10	19.61	0.65	0.02
Average				0.54	20.50				
SD				0.01	0.67				
Core 4 (0–2 cm)	1	2	10	0.54	20.4	2.43	0	0.54	0.02
Core 4 (2–4 cm)	3	8	20	0.53	20.0	1.75	2.43	0.44	0.01
Core 4 (4–6 cm)	5	16	30	0.54	20.2	2.15	4.18	0.49	0.02
Core 4 (6–8 cm)	7	18	40	0.52	19.3	1.76	6.34	0.47	0.01
Core 4 (8–10 cm)	9	21	50	0.53	19.9	0.44	8.09	–	–
Core 4 (10–12 cm)	11	23	60	0.53	19.8	2.20	8.54	–	–
Core 4 (12–15 cm)	13	25	70	0.53	19.7	0.00	10.74	–	–
Average				0.53	19.90				
SD				0.01	0.34				
Cumulative average					19.68				
Cumulative SD					0.79				

Table 2. Continued.

Sample	Eq. (4) excluding $\varphi+\theta+K$			Eq. (4) including $\varphi+\theta+K$		
	$_{SS+WC}TEX_{86}$ ($_{M}TEX_{86}$-$c(d_{0-n})^{*}_{Sed}TEX_{86}$)	$_{SS+WC}TEX^{H}_{86}$ (after Kim et al., 2010)	$_{SS+WC}TEX^{H}_{86}$ reconstructed SST (°C)	$\varphi+\theta$ (Eq. 6) (where $s^2 = 0.20$; Table S4)	$_{SS+WC}TEX_{86}$	$_{SS+WC}TEX^{H}_{86}$ reconstructed SST (°C) (after Kim et al., 2010)
Core 1 (0–2 cm)	0.56	−0.25	21.2	1.12	0.63	24.7
Core 1 (2–4 cm)	0.56	−0.25	21.4	1.12	0.63	24.9
Core 1 (4–6 cm)	0.54	−0.27	20.3	1.13	0.62	24.2
Core 1 (6–8 cm)	0.53	−0.27	19.8	1.13	0.61	23.9
Core 1 (8–10 cm)	0.52	−0.28	19.5	1.14	0.61	23.7
Core 1 (10–12 cm)	0.50	−0.30	17.9	1.15	0.58	22.6
Core 1 (12–15 cm)	0.53	−0.27	20.0	1.13	0.62	24.2
Core 1 (15–18 cm)	0.53	−0.27	19.8	1.13	0.61	24.1
Core 1 (18–21 cm)	0.55	−0.26	21.0	1.13	0.63	25.0
Average	0.54	−0.27	20.10	1.13	0.61	24.14
SD	0.02	0.02	1.08	0.01	0.02	0.75
Core 2 (0–2 cm)	0.55	−0.26	20.6	1.13	0.62	24.2
Core 2 (2–4 cm)	0.52	−0.28	19.2	1.14	0.60	23.3
Core 2 (4–6 cm)	0.51	−0.29	18.7	1.14	0.59	22.9
Core 2 (6–8 cm)	0.52	−0.28	19.3	1.14	0.60	23.4
Core 2 (8–10 cm)	0.53	−0.28	19.7	1.14	0.61	23.8
Core 2 (10–12 cm)	0.52	−0.28	19.1	1.14	0.60	23.4
Core 2 (12–15 cm)	0.51	−0.29	18.5	1.14	0.59	23.0
Core 2 (15–18 cm)	0.52	−0.28	19.2	1.14	0.60	23.5
Core 2 (18–21 cm)	0.52	−0.28	19.3	1.14	0.60	23.6
Average	0.52	−0.28	19.32	1.14	0.60	23.47
SD	0.01	0.01	0.60	0.00	0.01	0.40
Core 3 (0–2 cm)	0.52	−0.28	19.4	1.14	0.60	23.3
Core 3 (2–4 cm)	0.52	−0.28	19.4	1.14	0.60	23.3
Core 3 (4–6 cm)	0.53	−0.28	19.5	1.14	0.60	23.4
Core 3 (6–8 cm)	0.53	−0.27	19.9	1.13	0.60	23.6
Core 3 (8–10 cm)	0.52	−0.28	19.4	1.14	0.60	23.3
Core 3 (10–12 cm)	0.53	−0.28	19.6	1.14	0.60	23.5
Core 3 (12–15 cm)	0.55	−0.26	20.7	1.13	0.62	24.3
Core 3 (15–18 cm)	0.52	−0.28	19.3	1.14	0.60	23.4
Core3 (18–21 cm)	0.55	−0.26	21.0	1.13	0.62	24.6
Average	0.53	−0.27	19.79	1.14	0.60	23.64
SD	0.01	0.01	0.62	0.00	0.01	0.49
Core 4 (0–2 cm)	0.53	−0.27	19.8	1.13	0.60	23.6
Core 4 (2–4 cm)	0.53	−0.28	19.7	1.14	0.60	23.4
Core 4 (4–6 cm)	0.53	−0.28	19.8	1.14	0.60	23.5
Core 4 (6–8 cm)	0.52	−0.29	19.0	1.14	0.59	22.9
Core 4 (8–10 cm)	–	–	–	–	–	–
Core 4 (10–12 cm)	–	–	–	–	–	–
Core 4 (12–15 cm)	–	–	–	–	–	–
Average	0.53	−0.28	19.51	1.07	0.60	23.38
SD	0.01	0.01	0.38	0.00	0.01	0.31
Cumulative average			19.68			23.66
Cumulative SD			0.79			0.59

* Marks inherited values from the overlying sediment horizon.

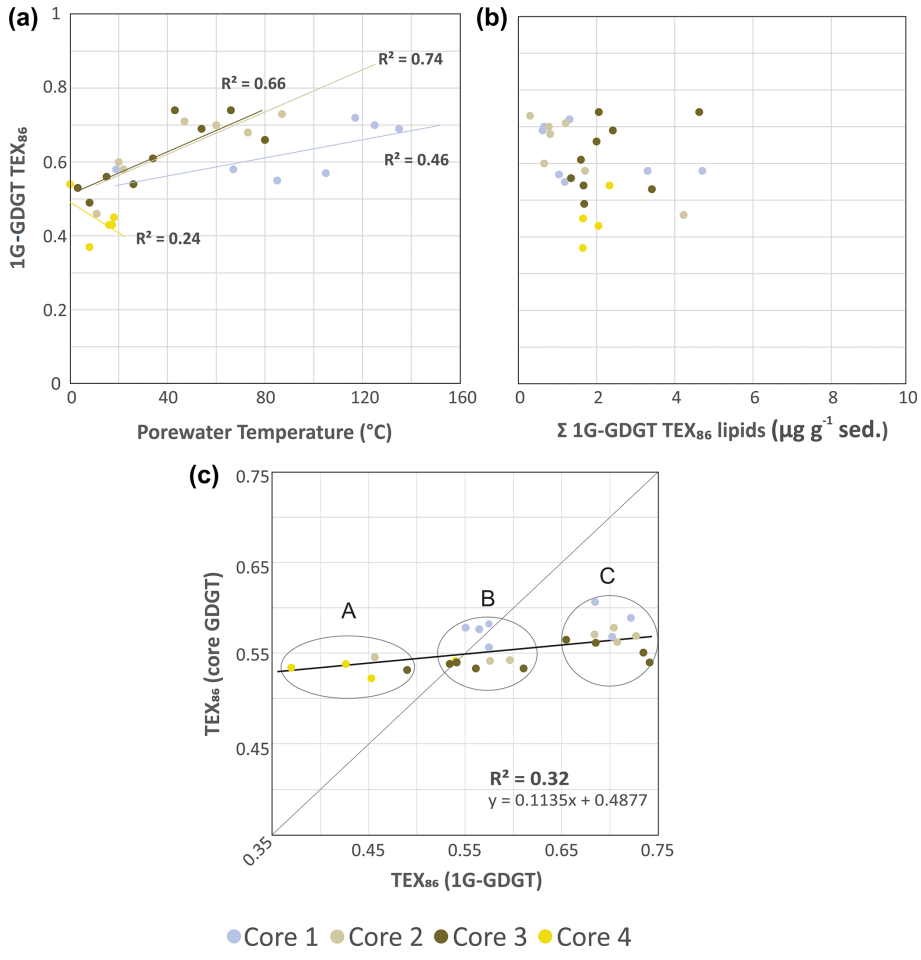

Figure 5. Cross plots of 1G-iGDGT $_{IPL}TEX_{86}$ versus **(a)** porewater temperatures and **(b)** the concentration of 1G-iGDGTs in the sediments. **(c)** TEX_{86} proxy for core GDGTs versus 1G-GDGTs. Clusters *A*–*C* may represent different archeal communities that are providing varying inputs of iGDGT to the core GDGT lipid pool. The dotted trend line is the partial least-square regression of the complete core lipid TEX_{86} data set. The solid line marks the 1 : 1 CL-to-IPL proxy correspondence indicating both allochthonous and autochthonous sources contribute equally to the core GDGT lipid pool.

The selective lipid removal by diagenetic and catagenetic processes theoretically may also affect the TEX_{86} value; however, their perspective impact on the directionality and magnitude of the ratio are difficult to predict and equally hard to discretely measure. Although the loss of GDGTs to protokerogen formation could potentially impact the ratio, it was shown to be a negligible sink for the lipids (Bentley et al., 2022). As such, the *K* parameter in Eqs. (3) and (4) was therefore assigned a 0 value. Due to the high geothermal gradient at Cathedral Hill, some of the transect push-core sediments resided within zones of active catagenesis (Fig. 2; Dalzell et al., 2021). The degradation rates of each TEX_{86} lipid were independently measured for the four push cores (Eq. 2; Fig. S2). As the abundance of both CLs and IPLs differentially decreases through the various core sediment profiles with turnover rates that appear to be constrained by porewater temperature changes (Sect. 3.1), the degradation rates must also record the effects of thermochemical oxidative weathering (Fig. 3b). In this case, φ and θ are treated as grouped parameters. To determine if individual lipid classes were selectively removed during degradation, the variance (s^2) of the rate change as measured from its respective regression slope (i.e., $m_{\log k'}$) from the TEX_{86} lipids (Fig. S2; Table S4 from Eq. 2) was calculated. For the Cathedral Hill transect, the calculated $m_{\log k'}$ s^2 is 0.20, which is due to accelerated degradation rates for higher-ring lipids, GDGT-3 and Cren', in samples from cores 1 and 2, where high vent temperatures resulted in hydrocarbon generation of the sediments (Dalzell et al., 2021). A weighing function for the degree of lipid class selectivity during turnover is proposed:

$$\varphi + \theta = \frac{1}{({}_{M}TEX_{86})^{s^2}}. \quad (6)$$

When applied to Eq. (4), the corrected data series produces an average transect $_{SS+WC}TEX_{86}^{H}$ reconstructed SST of $23.66 \pm 0.59\,^{\circ}C$ with a near-zero partial least-square re-

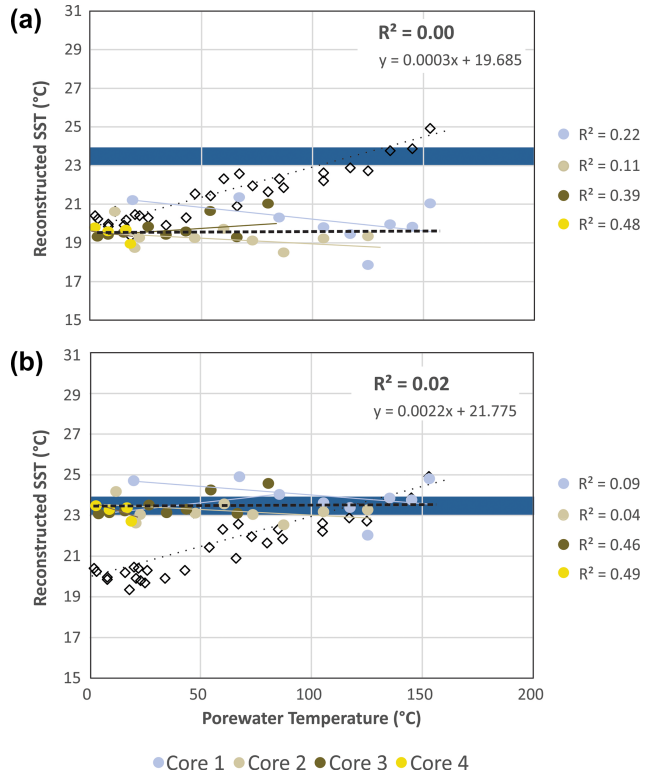

Figure 6. Reconstructed combined $_{SS}TEX_{86}$ and SST $_{WC}TEX_{86}$ from Eq. (4) **(a)** with and **(b)** without φ, K, and θ scaling parameters compared to measured porewater temperatures. Colored circles indicate recorded values from the four push cores. $_{M}TEX_{86}$ values are plotted for reference (open black diamonds). Blue field is the 23–24 °C range observed for the 21-year (1982–2004) satellite-derived MASST data (Herrera-Cervantes et al., 2007).

gression slope (Table 2; Fig. 6b). These modeled values are within the 23–24 °C obtained for the 21-year (1982–2004) satellite-derived MASST data for the Guaymas Basin region (Herrera-Cervantes et al., 2007). Based on these calculations, nearly all $_{M}TEX_{86}$ attenuation can be attributed to sediment microbial overprinting coupled to diagenetic and catagenetic loss of lipids consistent with prior observations at Guaymas Basin (Schouten et al., 2003; Zhang et al., 2011). The high degree of influence this has on the TEX_{86} proxy is striking given that the upper water flux of GDGTs at Cathedral Hill is estimated to represent up to 93 % of the total intact polar and core GDGT lipid pool within these sediments. Although, this study demonstrates the benthic microbial community can influence TEX_{86} values in anomalous, endmember environments, the above model has not yet been tested across conventional ocean shelf environments.

4 Conclusions

In this study, we demonstrate a pronounced overprint of cGDGTs sourced from the ocean floor sedimentary archaeal community at the Cathedral Hill vent site in Guaymas Basin. The overprint is marked by lipids with more cyclized ring moieties, marking an adaptive response by archaea to rigidify the cellular membranes against localized heat stress. This in turn has resulted in the commonly used TEX_{86} paleoclimate proxy partially recording advecting porewaters temperatures. As the vast majority of cGDGTs in these sediments is sourced from the overlying water column, the impact on the TEX_{86} ratio is further the product of rapid lipid turnover rates and diagenetic and catagenetic alteration processes potentially unique to the hydrothermal system. Together, these factors resulted in absolute TEX_{86}^{H} temperature offsets of up to 4 °C based on calibrations closely suited to the latitudinal position of Guaymas Basin. To untangle the impact of these coupled drivers on the TEX_{86} proxy, we further present a method to correct the overprints by both the water column and subsurface archaeal community using IPLs extracted from both of these sources. Although, we have not been able to test this model with lipid inputs from the overlying water column, we have demonstrated its effectiveness at removing sediment-sourced overprints, which may not be unique to hydrothermal systems. This approach should be capable of being extended to all near-surface marine sediment systems and may improve the quality of calibration models or climate reconstructions that are based on modern TEX_{86} measures.

Data availability. Data files are available by request.

Supplement. The supplement related to this article is available online at: https://doi.org/10.5194/bg-19-4459-2022-supplement.

Author contributions. JNB and GTV collected and provided analysis of the acquired data and carried out the conceptualization of the study. JNB was responsible for all chemical preparation of the samples. JNB, GTV, CCW, SMS, and JSS wrote the paper. All authors were involved with the review of various drafts as the paper developed across the peer-review process. GTV, SMS, and JSS provided funding for this project.

Competing interests. The contact author has declared that none of the authors has any competing interests.

Disclaimer. Publisher's note: Copernicus Publications remains neutral with regard to jurisdictional claims in published maps and institutional affiliations.

Acknowledgements. A special thank you is extended to associate editor Jack Middelburg and the *Biogeosciences* reviewers who provided highly constructive feedback. We are grateful to Carl Peters, formally at Saint Mary's University, who provided considerable feedback and advice during the course of this study. We further thank the officers, crew, and pilots of R/V *Atlantis* and HOV *Alvin* for their expert help at sea and their outstanding efforts acquiring the samples for this study. Julius Lipp, Florence Schubotz, and Kai-Uwe Hinrichs of MARUM (Center for Marine Environmental Sciences) assisted our lab in the development of lipidomic analytical techniques. Special thanks is extended to Clarissa Sit for the use of her HPLC–qToF-MS. Sean Sylvia assisted with the preparation of push cores used in sampling.

Financial support. This research has been supported by the Natural Sciences and Engineering Research Council of Canada (grant no. RGPIN-2018-06147; NSERC), NSERC Canada Research Chairs (CRC) program, Canada Foundation for Innovation (CFI; JELF–CRC, John R. Evans Leaders Fund), NSERC Discovery Grants program (application no. RGPIN-2017-05822), Woods Hole Oceanographic Institution (WHOI) Deep Ocean Exploration Initiative 2008, and Natural Science Foundation (grant no. MCB-0702677 to Jeffrey S. Seewald and Stefan M. Sievert; NSF).

Review statement. This paper was edited by Jack Middelburg and reviewed by three anonymous referees.

References

Bentley, J. N., Ventura, G. T., Dalzell, C. J., Walters, C. C., Peters, C. A., Mennito, A. S., Nelson, R. K., Reddy, C. M., Walters, C. J., Seewald, J., and Sievert, S. M.: Archaeal lipid diversity, alteration, preservation at Cathedral Hill, Guaymas Basin, and its link to the deep time preservation paradox, Org. Geochem., 163, 104302, https://doi.org/10.1016/j.orggeochem.2021.104302, 2022.

Besseling, M. A., Hopmans, E. C., Bale, N. J., Schouten, S., Sinninghe Damsté, J. S., and Villanueva, L.: The absence of intact polar lipid-derived GDGTs in marine waters dominated by Marine Group II: Implications for lipid biosynthesis in Archaea, Sci. Rep., 10, 294, https://doi.org/10.1038/s41598-019-57035-0, 2020.

Besseling, M., Hopmans, E. C., Koenen, M., van der Meer, M. T. J., Vreugdenhil, S., Schouten, S., Sinninghe Damsté, J. S., and Villanueva, L.: Depth-related differences in archaeal populations impact the isoprenoid tetraether lipid composition of the Mediterranean Sea water column, Org. Geochem., 135, 16–31, https://doi.org/10.1016/j.orggeochem.2019.06.008, 2019.

Biddle, J. F., Cardman, Z., Mendlovitz, H., Albert, D. B., Lloyd, K. G., Boetius, A., and Teske, A.: Anaerobic oxidation of methane at different temperature regimes in Guaymas Basin hydrothermal sediments, ISME J., 6, 1018–1031, https://doi.org/10.1038/ismej.2011.164, 2012.

Boetius, A., Ravenschlag, K., Schubert, C., Rickert, D, Widdel, F., Gieseke, A., Amann, R., Jørgensen, B. B., Witte, U., and Pfannkuche, O.: A marine microbial consortium apparently mediating anaerobic oxidation of methane, Nature, 407, 623–626, https://doi.org/10.1038/35036572, 2000.

Boyd, E., Hamilton, T., Wang, J., He, L., and Zhang, C.: The role of tetraether lipid composition in the adaptation of thermophilic archaea to acidity, Front. Microbiol., 4, 62, https://doi.org/10.3389/fmicb.2013.00062, 2013.

Brassell, S. C., Eglinton, G., Marlowe, I. T., Pflaumann, U., and Sarnthein, M.: Molecular stratigraphy: a new tool for climatic assessment, Nature, 320, 129–133, https://doi.org/10.1038/320129a0, 1986.

Brochier-Armanet, C., Boussau, B., Gribaldo, S., and Forterre, P.: Mesophilic Crenarchaeota: proposal for a third archaeal phylum, the Thaumarchaeota, Nat. Rev. Microbiol., 6, 245–252, https://doi.org/10.1038/nrmicro1852, 2008.

Carr, S. A., Schubotz, F., Dunbar, R. B., Mills, C. T., Dias, R., Summons, R. E., and Mandernack, K. W.: Acetoclastic Methanosaeta are dominant methanogens in organic-rich Antarctic marine sediments, ISME J., 12, 330–342, https://doi.org/10.1038/ismej.2017.150, 2018.

Dalzell, C. J., Ventura, G. T., Nelson, R. K., Reddy, C. M., Walters, C. J., Seewald, J., and Sievert, S. M.: Resolution of multi-molecular hydrocarbon transformation in petroleum-bearing sediments from the Cathedral Hill hydrothermal vent complex at Guaymas Basin, Gulf of California by comprehensive two-dimensional gas chromatography and chemometric analyses, Org. Geochem., 152, 104173, https://doi.org/10.1016/j.orggeochem.2020.104173, 2021.

De Rosa, M. and Gambacorta, A.: The lipids of archaebacteria, Pro. Lipid Res., 27, 153–175, https://doi.org/10.1016/0163-7827(88)90011-2, 1988.

Elling, F. J., Könneke, M., Lipp, J. S., Becker, K. W., Gagen, E. J., and Hinrichs, K.-U.: Effects of growth phase on the membrane lipid composition of the thaumarchaeon *Nitrosopumilus maritimus* and their implications for archaeal lipid distributions in the marine environment, Geochim. Cosmochim. Ac., 141, 579–597, https://doi.org/10.1016/j.gca.2014.07.005, 2014.

Elling, F. J., Könneke, M., Mußmann, M., Greve, A., and Hinrichs, K. U.: Influence of temperature, pH, and salinity on membrane lipid composition and TEX_{86} of marine planktonic thaumarchaeal isolates, Geochim. Cosmochim. Ac., 171, 238–255, https://doi.org/10.1016/j.gca.2015.09.004, 2015.

Gieskes, J. M., Simoneit, B. R., Brown, T., Shaw, T. J., Wang, Y. C., and Magenheim, A.: Hydrothermal fluids and petroleum in surface sediments of Guaymas Basin, Gulf of California: a case study, Can. Mineral., 26, 589–602, 1988.

Gliozzi, A., Paoli, G., De Rosa, M., and Gambacorta, A.: Effect of isoprenoid cyclization on the transition temperature of lipids in thermophilic archaebacteria, Biochim. Biophys. Acta (BBA)-Biomembranes, 735, 234–242, https://doi.org/10.1016/0005-2736(83)90298-5, 1983.

Herfort, L., Schouten, S., Boon, J. P., and Sinninghe Damsté, J. S.: Application of the TEX86 temperature proxy to the southern North Sea, Org. Geochem., 37, 1715–26, https://doi.org/10.1016/j.orggeochem.2006.07.021, 2006.

Herrera-Cervantes, H., Lluch-Cota, D. B., Lluch-Cota, S. E., and Gutiérrez-de-Velasco, S. G.: The ENSO signature in sea-surface temperature in the Gulf of California, J. Mar. Res., 65, 589–605, https://doi.org/10.1357/002224007783649529, 2007.

Hollis, C. J., Taylor, K. W. R., Handley, L., Pancost, R. D., Huber, M., Creech, J. B., Hines, B. R., Crouch, E. M., Morgans, H. E. G., Crampton, J. S., Gibbs, S., Pearson, P. N., and Zachos, J. C. Early Paleogene temperature history of the Southwest Pacific Ocean: Reconciling proxies and models, Earth Planetary Sci. Lett., 349–350, 53–66, https://doi.org/10.1016/j.epsl.2012.06.024, 2012.

Ho, S. L. and Laepple, T.: Flat meridional temperature gradient in the early Eocene in the subsurface rather than surface ocean, Nat. Geosci., 9, 606–610, https://doi.org/10.1038/ngeo2763, 2016.

Hopmans, E. C., Weijers, J. W., Schefuß, E., Herfort, L., Sinninghe Damsté, J. S., and Schouten, S.: A novel proxy for terrestrial organic matter in sediments based on branched and isoprenoid tetraether lipids, Earth Planetary Sci. Lett., 224, 107–116, https://doi.org/10.1016/j.epsl.2004.05.012, 2004.

Huguet, C., Cartes, J. E., Sinninghe Damsté, J. S., and Schouten, S.: Marine crenarchaeotal membrane lipids in decapods: Implications for the TEX_{86} paleothermometer, Geochem. Geophys. Geosyst., 7, Q11010, https://doi.org/10.1029/2006GC001305, 2006.

Huguet, C., Schimmelmann, A., Thunell, R., Lourens, L. J., Sinninghe Damsté, J. S., and Schouten, S.: A study of the TEX_{86} paleothermometer in the water column and sediments of the Santa Barbara Basin, California, Paleoceanography, 22, PA3203, https://doi.org/10.1029/2006PA001310, 2007.

Huguet, C., Martrat, B., Grimalt, J. O., Sinninghe Damsté, J. S., and Schouten, S.: Coherent millennial-scale patterns in $U^{k'}_{37}$ and TEX^{H}_{86} temperature records during the penultimate interglacial-to-glacial cycle in the western Mediterranean, Paleoceanography, 22, PA2218, https://doi.org/10.1029/2010PA002048, 2011.

Hurley, S. J., Elling, F. J., Könneke, M., Buchwald, C., Wankel, S. D., Santoro, A. E., Lipp, J. S., Hinrichs, K.-U., and Pearson, A.: Influence of ammonia oxidation rate on thaumarchaeal lipid composition and the TEX_{86} temperature proxy, P. Natl. Acad. Sci. USA., 113, 7762–7767, https://doi.org/10.1073/pnas.1518534113, 2016.

Kallmeyer, J. and Boetius, A.: Effects of temperature and pressure on sulfate reduction and anaerobic oxidation of methane in hydrothermal sediments of Guaymas Basin, Appl. Environ. Microbiol., 70, 1231–1233, https://doi.org/10.1128/AEM.70.2.1231-1233.2004, 2004.

Karner, M. B., DeLong, E. F., and Karl, D. M.: Archaeal dominance in the mesopelagic zone of the Pacific Ocean, Nature, 25, 507–510, https://doi.org/10.1038/35054051, 2001.

Kashefi, K. and Lovley, D. R.: Extending the upper temperature limit for life, Science, 301, 934–934, https://doi.org/10.1126/science.1086823, 2003.

Kim, J. H., Schouten, S., Hopmans, E. C., Donner, B., and Sinninghe Damsté, J. S.: Global sediment core-top calibration of the TEX_{86} paleothermometer in the ocean, Geochim. Cosmochim. Ac., 72, 1154–1173, https://doi.org/10.1016/j.gca.2007.12.010, 2008.

Kim, J. H., Van der Meer, J., Schouten, S., Helmke, P., Willmott, V., Sangiorgi, F., Koç, N., Hopmans, E. C., and Sinninghe Damsté, J. S.: New indices and calibrations derived from the distribution of crenarchaeal isoprenoid tetraether lipids: Implications for past sea surface temperature reconstructions, Geochim. Cosmochim. Ac., 74, 4639–4654, https://doi.org/10.1016/j.gca.2010.05.027, 2010.

Kim, J.-H., Romero, O. E., Lohmann, G., Donner, B., Laepple, T., Haam, E., and Sinninghe Damsté, J. S.: Pronounced subsurface cooling of North Atlantic waters off Northwest Africa during Dansgaard-Oeschger interstadials, Earth Planetary Sci. Lett., 339–340, 95–102, https://doi.org/10.1016/j.epsl.2012.05.018, 2012a.

Kim, J.-H., Crosta, X., Willmott, V., Renssen, H., Bonnin, J., Helmke, P., Schouten, S., and Sinninghe Damsté, J. S.: Holocene subsurface temperature variability in the eastern Antarctic continental margin, Geophys. Res. Lett., 39, L06705, https://doi.org/10.1029/2012GL051157, 2012b.

Kim J.-H., Schouten, S., Rodrigo-Gamiz, M., Rampen, S., Marino, G., Huguet, C., Helmke, P., Buscail, R., Hopmans, E. C., Pross, J., Sangiorgi, F., Middelburg, J. B. M., and Sinninghe Damsté, J. S.: Influence of deep-water derived isoprenoid tetraether lipids on the paleothermometer in the Mediterranean Sea, Geochim. Cosmochim. Ac., 150, 125–141, https://doi.org/10.1016/j.gca.2014.11.017, 2015.

Knappy, C. S., Chong, J. P., and Keely, B. J.: Rapid discrimination of archaeal tetraether lipid cores by liquid chromatography-tandem mass spectrometry, J. Am. Soc. Mass Spectr., 20, 51–59, https://doi.org/10.1016/j.jasms.2008.09.015, 2009.

Lawrence, K. T., Pearson, A., Castaneda, I. S., Ladlow, C., Peterson, L. C., and Lawrence, G. E.: Comparison of Late Neogene $U^{k'}_{37}$ and TEX_{86} Paleotemperature records from the eastern equatorial Pacific at orbital resolution, Paleoceanogr. Paleoclimatol., 35, 1–16, https://doi.org/10.1029/2020PA003858, 2020.

Lengger, S. K., Hopmans, E. C., Reichart, G.-J., Nierop, K. G. J., Sinninghe Damsté, J. S., and Schouten, S.: Intact polar and core glycerol dibiphytanyl glycerol tetraether lipids in the Arabian Sea oxygen minimum zone. Part II: Selective preservation and degradation in sediments and consequences for the TEX_{86}, Geochim. Cosmochim. Ac., 98, 244–258, https://doi.org/10.1016/j.gca.2012.05.003, 2012.

Lengger, S. K., Hopmans, E. C., Sinninghe Damsté, J. S., and Schouten, S.: Fossilization and degradation of archaeal intact polar tetraether lipids in deeply buried marine sediments (Peru Margin), Geobiology, 12, 212–220, https://doi.org/10.1111/gbi.12081, 2014.

Lipp, J. S. and Hinrichs, K. U.: Structural diversity and fate of intact polar lipids in marine sediments, Geochim. Cosmochim. Ac., 73, 6816–6833, https://doi.org/10.1016/j.gca.2009.08.003, 2009.

Liu, X. L., Leider, A., Gillespie, A., Gröger, J., Versteegh, G. J., and Hinrichs, K. U.: Identification of polar lipid precursors of the ubiquitous branched GDGT orphan lipids in a peat bog in Northern Germany, Org. Geochem., 41, 653–660, https://doi.org/10.1016/j.orggeochem.2010.04.004, 2010.

Liu, X. L., Russell, D. A., Bonfio, C., and Summons, R. E.: Glycerol configurations of environmental GDGTs investigated using a selective sn2 ether cleavage protocol, Org. Geochem., 128, 57–62, https://doi.org/10.1016/j.orggeochem.2018.12.003, 2018.

Lopes dos Santos, R. A., Prange, M., Castañeda, I. S., Schefuß, E., Mulitza, S., Schulz, M., Niedermeyer, E. M., Sinninghe Damsté, J. S., and Schouten S.: Glacial–interglacial variability in Atlantic meridional overturning circulation and thermocline adjustments in the tropical North Atlantic, Earth Planetary Sci. Lett., 300, 407–414, https://doi.org/10.1016/j.epsl.2010.10.030, 2010.

Lunt, D. J., Haywood, A. M., Schmidt, G. A., Salzmann, U., Valdes, P. J., Dowsett, H. J., and Loptson, C. A.:

On the causes of mid-Pliocene warmth and polar amplification, Earth Planetary Sci. Lett., 321–322, 128–138, https://doi.org/10.1016/j.epsl.2011.12.042, 2012.

Macalady, J. L., Vestling, M. M., Baumler, D., Boekelheide, N., Kaspar, C. W., and Banfield, J. F.: Tetraether-linked membrane monolayers in *Ferroplasma* spp: a key to survival in acid, Extremophiles, 8, 411–419, https://doi.org/10.1007/s00792-004-0404-5, 2004.

McClymont, E. L., Ganeshram, R. S., Pichevin, L. E., Talbot, H. M., van Dongen, B. E., Thunell, R. C., Haywood, A. M., Singarayer, J. S., and Valdes, P. J.: Sea-surface temperature records of Termination 1 in the Gulf of California: Challenges for seasonal and interannual analogues of tropical Pacific climate change, Paleoceanography, 27, PA2202, https://doi.org/10.1029/2011PA002226, 2012.

McKay, L. J., MacGregor, B. J., Biddle, J. F., Albert, D. B., Mendlovitz, H. P., Hoer, D. R., Lipp, J. S., Lloyd, K. G., and Teske, A. P.: Spatial heterogeneity and underlying geochemistry of phylogenetically diverse orange and white *Beggiatoa* mats in Guaymas Basin hydrothermal sediments, Deep-Sea Res. Pt. I, 67, 21–31, https://doi.org/10.1016/j.dsr.2012.04.011, 2012.

Meyer, S., Wegener, G., Lloyd, K. G., Teske, A., Boetius, A., and Ramette, A.: Microbial habitat connectivity across spatial scales and hydrothermal temperature gradients at Guaymas Basin, Front. Microbiol., 4, 207, https://doi.org/10.3389/fmicb.2013.00207, 2013.

Naafs, B. D. A., Rohrssen, M., Inglis, G. N., Lähteenoja, O., Feakins, S. J., Collinson, M. E., Kennedy, E. M., Singh, P. K., Singh, M. P., Lunt, D. J., and Pancost, R. D.: High temperatures in the terrestrial mid-latitudes during the early Palaeogene, Nat. Geosci., 11, 766–771, https://doi.org/10.1038/s41561-018-0199-0, 2018.

O'Brien, C. L., Robinson, S. A. Pancost, R. D., Sinninghe Damste, J. S., Schouten, S., Lunt, D. J., Alsenz, H., Bomemann, A., Bottini, C., Brassell, S. C., Farnsworth, A., Forster, A., Huber, B. T., Inglis, G. N., Jenkyns, H. C., Linnert, C., Littler, K., Markwick, P., McAnena, A., Mutterlose, J., Naafs, B. D. A., Puttmann, W., Sluijs, A., van Helmond, N. A. G. M., Vellekoop, J., Wagner, T., and Wrobel, N. E.: Cretaceous sea-surface temperature evolution: Constraints from TEX_{86} and planktonic foraminiferal oxygen isotopes, Earth Sci. Rev., 172, 224–247, https://doi.org/10.1016/j.earscirev.2017.07.012, 2017.

Pearson, A. and Ingalls, A. E.: Assessing the use of archaeal lipids as marine environmental proxies, Annu. Rev. Earth Planet. Sci., 41, 359–384, https://doi.org/10.1146/annurev-earth-050212-123947, 2013.

Pearson, A., Huang, Z., Ingalls, A. E., Romanek, C. S., Wiegel, J., Freeman, K. H., Smittenberg, R. H., and Zhang, C. L.: Nonmarine crenarchaeol in Nevada hot springs, Appl. Environ. Microbiol., 70, 5229–5237, https://doi.org/10.1128/AEM.70.9.5229-5237.2004, 2004.

Petrick, B., Reuning, L., and Martinez-Garcia: Distribution of Glycerol Dialkyl Glycerol Tetraethers (GDGTs) in Microbial Mats from Holocene and Miocene Sabkha Sediments, Front. Earth Sci., 7, 310, https://doi.org/10.3389/feart.2019.00310, 2019.

Qin, W., Carlson, L. T., Armbrust, E. V., Devol, A. H., Moffett, J. W., Stahl, D. A., and Ingalls, A. E.: Confounding effects of oxygen and temperature on the TEX_{86} signature of marine Thaumarchaeota, P. Natl. Acad. Sci. USA., 112, 10,979–10,984. https://doi.org/10.1073/pnas.1501568112, 2015.

Rommerskirchen, F., Condon, T., Mollenhauer, G., Dupont, L. M., and Schefuß, E.: Miocene to Pliocene development of surface and subsurface temperatures in the Benguela Current system, Paleoceanography, 26, 1–15, https://doi.org/10.1029/2010PA002074, 2011.

Schouten, S., Hopmans, E. C., Schefuß, E., and Sinninghe Damsté, J. S.: Distributional variations in marine crenarchaeotal membrane lipids: a new tool for reconstructing ancient sea water temperatures?, Earth Planetary Sci. Lett., 204, 265–274, https://doi.org/10.1016/S0012-821X(02)00979-2, 2002.

Schouten S., Wakeham S. G., Hopmans E. C., and Sinninghe Damsté, J. S.: Biogeochemical Evidence that Thermophilic Archaea Mediate the Anaerobic Oxidation of Methane, Appl. Environ. Microbiol., 69, 1680–1686, https://doi.org/10.1128/AEM.69.3.1680-1686.2003, 2003.

Schouten, S., Hopmans, E. C., and Sinninghe Damsté, J. S.: The effect of maturity and depositional redox conditions on archaeal tetraether lipid palaeothermometry, Org. Geochem., 35, 567–571, https://doi.org/10.1016/j.orggeochem.2004.01.012, 2004.

Schouten, S., Middelburg, J. J., Hopmans, E. C., and Sinninghe Damsté, J. S.: Fossilization and degradation of intact polar lipids in deep subsurface sediments: a theoretical approach, Geochim. Cosmochim. Ac., 74, 3806–3814, https://doi.org/10.1016/j.gca.2010.03.029, 2010.

Schouten, S., Hopmans, E. C., and Sinninghe Damsté, J. S.: The organic geochemistry of glycerol dialkyl glycerol tetraether lipids: A review, Org. Geochem., 54, 19–61, https://doi.org/10.1016/j.orggeochem.2012.09.006, 2013.

Seki, O., Schmidt, D. N., Schouten, S., Hopmans, E. C., Sinninghe Damsté, J. S., and Pancost, R. D.: Paleoceanographic changes in the Eastern Equatorial Pacific over the last 10 Myr., Paleoceanography, 27, PA3224, https://doi.org/10.1029/2011PA002158, 2012.

Seki, O., Bendle, J. A., Haranda, N., Kobayashi, M., Sawada, K., Moossen, H., Inglis, G. N., Nagao, S., and Sakamoto, T.: Assessment and calibration of TEX_{86} paleothermometry in the Sea of Okhotsk and sub-polar North Pacific region: Implications for paleoceanography, Prog. Oceanogr., 126, 254–266, https://doi.org/10.1016/j.pocean.2014.04.013, 2014.

Sinninghe Damsté, J. S., Rijpstra, W. I. C., Hopmans, E. C., den Uijl, M. J., Weijers, J. W. H., and Schouten S.: The enigmatic structure of the crenarchaeol isomer, Org. Geochem., 124, 22–28, https://doi.org/10.1016/j.orggeochem.2018.06.005, 2018.

Stadnitskaia, A., Nadezhkin, D., Abbas, B., Blinova, V., Ivanov, M. K., and Sinninghe Damsté, J. S.: Carbonate formation by anaerobic oxidation of methane: evidence from lipid biomarker and fossil 16S rDNA, Geochim. Cosmochim. Ac., 72, 1824–1836, https://doi.org/10.1016/j.gca.2008.01.020, 2008.

Sturt, H. F., Summons, R. E., Smith, K., Elvert, M., and Hinrichs, K. U.: Intact polar membrane lipids in prokaryotes and sediments deciphered by high-performance liquid chromatography/electrospray ionization multistage mass spectrometry – new biomarkers for biogeochemistry and microbial ecology, Rapid Commun. Mass Spectrom., 18, 617–628, https://doi.org/10.1002/rcm.1378, 2004.

Teske, A., De Beer, D., McKay, L. J., Tivey, M. K., Biddle, J. F., Hoer, D., Lloyd, K. G., Lever, M. A., Røy, H., Albert, D. B., and

MacGregor, B. J.: The Guaymas Basin hiking guide to hydrothermal mounds, chimneys, and microbial mats: Complex seafloor expressions of subsurface hydrothermal circulation, Front. Microbiol., 7, 75, https://doi.org/10.3389/fmicb.2016.00075, 2016.

Tierney, J. E.: Biomarker-based inferences of past climate: the TEX_{86} paleotemperature proxy, in: Treatise on Geochemistry, 2nd edn., edited by: Holland, H. D. and Turekian, K. K., Geochemistry, 2nd edn., Elsevier, vol. 12, 379–939, https://doi.org/10.1016/B978-0-08-095975-7.01032-9, 2014.

Uda, I., Sugai, A., Itoh, Y. H., and Itoh, T.: Variation in molecular species of polar lipids from *Thermoplasma acidophilum* depends on growth temperature, Lipids, 36, 103–105, https://doi.org/10.1007/s11745-001-0914-2, 2001.

Umoh, U., Li, L., Luckge, A., Schwartz-Schampera, U., and Naafs, D.: Influence of hydrothermal vent activity on GDGT pool in marine sediments might be less than previously thought, Org. Geochem., 149, 104102, https://doi.org/10.1016/j.orggeochem.2020.104102, 2020.

Wakeham, S. G., Lewis, C. M., Hopmans, E. C., Schouten, S., and Sinninghe Damsté, J. S.: Archaea mediate anaerobic oxidation of methane in deep euxinic waters of the Black Sea, Geochim. Cosmochim. Ac., 67, 1359–1374, https://doi.org/10.1016/S0016-7037(02)01220-6, 1359–1374, 2003.

Weijers, J. W., Schouten, S., van den Donker, J. C., Hopmans, E. C., and Sinninghe Damsté, J. S.: Environmental controls on bacterial tetraether membrane lipid distribution in soils, Geochim. Cosmochim. Ac., 71, 703–713, https://doi.org/10.1016/j.gca.2006.10.003, 703–713, 2007.

Weijers, J. W., Schefuß, E., Kim, J. H., Sinninghe Damsté, J. S., and Schouten, S.: Constraints on the sources of branched tetraether membrane lipids in distal marine sediments, Org. Geochem., 72, 14–22, https://doi.org/10.1016/j.orggeochem.2014.04.011, 2014.

Wuchter, C., Schouten, S., Wakeham, S. G., and Sinninghe Damsté, J. S.: Temporal and spatial variation in tetraether membrane lipids of marine Crenarchaeota in particulate organic matter: Implications for TEX_{86} paleothermometry, Paleoceanography, 20, PA3013, https://doi.org/10.1029/2004PA001110, 2005.

Wuchter, C., Schouten, S., Wakeham, S. G., and Sinninghe Damsté, J. S.: Archaeal tetraether membrane lipid fluxes in the northeastern Pacific and the Arabian Sea: implications for TEX_{86} paleothermometry, Paleoceanography, 21, PA4208, https://doi.org/10.1029/2006PA001279, 2006.

Xie, S., Lipp, J. S., Wegener, G., Ferdelman, T. G., and Hinrichs, K.-U.: Turnover of microbial lipids in the deep biosphere and growth of benthic archaeal populations, P. Natl. Acad. Sci, USA, 110, 6010–6014, https://doi.org/10.1073/pnas.1218569110, 2013.

Yoshinaga, M. Y., Kellermann, M. Y., Rossel, P. E., Schubotz, F., Lipp, J. S., and Hinrichs, K. U.: Systematic fragmentation patterns of archaeal intact polar lipids by high-performance liquid chromatography/electrospray ionization ion-trap mass spectrometry, Rap. Commun. Mass Spectrom., 25, 3563–3574, https://doi.org/10.1002/rcm.5251, 2011.

Zeng, Z., Liu, X. L., Farley, K. R., Wei, J. H., Metcalf, W. W., Summons, R. E., Zhang, Y. G., Pagani, M., and Wang, Z.: Ring Index: A new strategy to evaluate the integrity of TEX_{86} paleothermometry, Paleoceanogr. Paleoclimatol., 31, 220–232, https://doi.org/10.1002/2015PA002848, 2016.

Zhang, Y. G., Zhang, C. L., Liu, X. L., Li, L., Hinrichs, K. U., and Noakes, J. E.: Methane Index: A tetraether archaeal lipid biomarker indicator for detecting the instability of marine gas hydrates, Earth Planetary Sci. Lett., 307, 525–534, https://doi.org/10.1016/j.epsl.2011.05.031, 2011.

Zhang, Y. G., Pagani, M., and Wang, Z.: Ring Index: A new strategy to evaluate the integrity of TEX_{86} paleotherm, Paleoceanograph. Paleoclim., 31, 220–232, https://doi.org/10.1002/2015PA002848, 2016.

Zhu, C., Lipp, J. S., Wörmer, L., Becker, K. W., Schröder, J., and Hinrichs, K. U.: Comprehensive glycerol ether lipid fingerprints through a novel reversed phase liquid chromatography-mass spectrometry protocol, Org. Geochem., 65, 53–62, https://doi.org/10.1016/j.orggeochem.2013.09.012, 2013.